

Multi-year surface radiative properties and vegetation parameters for hydrologic modeling in regions of complex terrain—Methodology and evaluation over the Integrated Precipitation and Hydrology Experiment 2014 domain

Jing Tao¹, Ana P. Barros*

Department of Civil & Environmental Engineering, Pratt School of Engineering, Duke University, Durham, NC, 27708, United States



ARTICLE INFO

Keywords:

Water cycle
Surface fluxes
Emissivity
Albedo
Vegetation parameters

ABSTRACT

Study region: Southeast US (SE US).

Study focus: This study probes the propagation of errors in standard remote-sensing vegetation products caused by cloud contamination and the impact of time-variant radiative properties for correctly describing land-surface properties in hydrologic models. Spatiotemporally-varying quality-controlled vegetation attributes (i.e., leaf area index and fractional vegetation coverage) and surface radiative properties (i.e., longwave broadband emissivity and shortwave broadband albedo) were derived from MODIS (Moderate Resolution Imaging Spectroradiometer) products over the SE US at 1 km × 1 km and hourly resolutions from 2007 to 2013. The data sets are publicly available. The impact of uncorrected standard vegetation products and static treatments of radiative properties was assessed systematically clearly illustrating improvements in simulated water and energy fluxes using the developed landscape attributes with a fully-distributed uncalibrated hydrologic model.

New hydrological insights for the region: Through simulations in the Southern Appalachian Mountains, we found that the spatiotemporal variability of radiative properties significantly influences the diurnal cycle of the surface energy budget with marked differences in sensible heat fluxes (up to 10–20%). Better performance of streamflow simulations achieved by using the improved vegetation attributes is tied to changes in rainfall interception and evapotranspiration, reflecting the importance of SE forests in the regional water cycle. The largest improvements in streamflow simulations result from larger corrections to MODIS products in the inner mountain region where cloudiness is persistent.

1. Introduction

Surface radiative properties (e.g. shortwave broadband albedo and longwave broadband emissivity) and vegetation characteristics (e.g., leaf area index (LAI) and fractional vegetation coverage (FVC)) are key parameters describing land surface boundary and thus modulating water and energy fluxes at the soil-vegetation-atmosphere interface (Koster and Suarez, 1992; Sellers et al., 1996).

* Corresponding author.

E-mail address: barros@duke.edu (A.P. Barros).

¹ Currently at Climate and Ecosystem Sciences Division, Lawrence Berkeley National Laboratory, Berkeley, CA 94720, United States, and Department of Civil & Environmental Engineering, University of Washington, Seattle, WA 98195, United States.

Land surface albedo and emissivity govern the radiation budget and consequently impact sensible and latent heat fluxes, and ultimately land-surface temperature at the field scales relevant for hydrologic modeling (e.g., [Dash et al., 2002](#); [Schmugge et al., 2002](#); [Trigo et al., 2008](#); [Wan and Li, 1997](#)). LAI and FVC scale latent and sensible heat fluxes (and carbon fluxes) from the point to the grid scale, and significantly affect the hydrologic cycle through impacting rainfall interception, canopy evapotranspiration, throughfall and stemflow, soil moisture and eventually streamflow response (e.g., [Das et al., 2018](#); [Galdos et al., 2012](#); [Marin et al., 2000](#); [Park and Cameron, 2008](#); [Yildiz and Barros, 2005,2007](#)).

Generally, vegetation characteristics should vary both in space and time according to regional phenology along with changes in spatial patterns and vegetation composition due to anthropogenic or natural disturbances (e.g., forest thinning and other management practices, high winds, landslides, wildfires ([Brun and Barros, 2013](#))). A recent study by [Das et al. \(2018\)](#) suggested that LAI is the most sensitive vegetation parameter reflecting land use and land cover change (e.g., deforestation, urbanization, and cropland expansions), and thus altering regional water balance at a decadal scale. However, not until recently most land surface models (LSMs) and hydrologic models still use static vegetation properties assigned according to land cover types (i.e., land-cover-dependent) or multi-year averaged monthly climatology of satellite-derived vegetation properties (i.e., climatologically-based) to prescribe the land surface boundary. The baseline “Noah” LSM ([Chen et al., 1997](#); [Ek et al., 2003](#); [Mahrt and Ek, 1984](#); [Mahrt and Pan, 1984](#); [Mitchell et al., 2004](#); [Pan and Mahrt, 1987](#)) exemplifies early-stage LSMs that use static land-cover-dependent LAI data (e.g., derived from AVHRR (Advanced Very High Resolution Radiometer) ([Kaufmann et al., 2000](#))). Later, many models use climatologically-based monthly LAI (i.e., static seasonality without inter-annual variability) usually averaged from standard products derived from optical satellite sensors such as the AVHRR (e.g., used in the Variable Infiltration Capacity (VIC) hydrologic model ([Liang et al., 1994](#)), in the Land-Surface Hydrology Model (LSHM) ([Devonec and Barros, 2002](#)), and in the NASA’s Land Information System (LIS) ([Kumar et al., 2006](#))), MODIS (Moderate Resolution Imaging Spectroradiometer) (e.g., used in NASA’s LIS, NASA’s Catchment Land Surface Model (CLSM) ([Ducharme et al., 2000](#); [Koster et al., 2000](#); [Mahanama et al., 2015](#)), and NCEP’s Multi-Physics (MP) version of the Noah model (Noah-MP) ([Niu et al., 2011](#))), and Landsat TM/ETM+ (Thematic Mapper/Enhanced Thematic Mapper Plus) (e.g., used in a distributed hydrological model at watershed scale ([Chen et al., 2005](#))).

Previously much attention already has been paid to investigate the hydrological impact of dynamic vegetation properties. For instance, [Lawrence and Slingo \(2004\)](#) found that the seasonality of latent heat fluxes and surface temperature are strongly affected by seasonally varying LAI. Similarly, [Kumar et al. \(2014\)](#) reported significant improvements in simulations of energy fluxes by replacing land-cover-dependent vegetation data and climatologically-based vegetation data at low resolution (0.144°, or approximately 15 km) used in the Noah model with the standard MODIS 8-day products at relatively high spatial resolution (1 km) for a four-day simulation. Regarding the impacts of dynamic vegetation characteristics on water flux simulations, previous work showed that the joint space-time distribution of FVC and LAI are essential to capture the seasonality and inter-annual variability of streamflow in hydrologic models ([Yildiz and Barros, 2005, 2007, 2009](#)). Specifically, [Yildiz and Barros \(2007\)](#) first implemented direct assimilation of time-varying vegetation by deriving their own LAI and FVC products from AVHRR NDVI (Normalized Difference Vegetation Index) in the LSHM for continuous 6-month simulations of spring-summer conditions under dry and wet hydrometeorological regimes. Inter-comparison studies also demonstrated that using time-varying vegetation characteristics can improve the simulations of soil moisture ([Ford and Quiring, 2013](#)) and streamflow ([Andersen et al., 2002](#); [Tesemma et al., 2015](#)) by contrasting the results against conventionally static LAI. The impact on the coupled water-carbon cycle was recently examined by [Lowman and Barros \(2018\)](#) who introduced prognostic phenology into an existing implementation of the LSHM with dynamic vegetation ([Garcia-Quijano and Barros, 2005](#)). They showed that model vegetation develops adaptation water-use strategies in response to seasonal and inter-annual climate variations that feedback nonlinearly into soil moisture and Gross Primary Productivity (GPP).

Despite the growing awareness of the need to use time-varying vegetation characteristics, few hydrologic models prescribe vegetation conditions using real-time dynamic vegetation products with realistic inter- and intra-annual variability due to the lack of continuous/gap-free time-varying vegetation products at a high temporal resolution. A major challenge in addressing this impasse is the combination of retrieval uncertainty, systematic errors and data gaps in optical remote-sensing products (e.g., AVHRR, MODIS, etc.) caused by cloud/fog (and precipitation) contamination as extensively documented in the literature ([Gao et al., 2008](#); [Lopez-Burgos et al., 2013](#); [Román et al., 2009](#); [Williamson et al., 2013](#); [Yang et al., 2007](#); [Yuan et al., 2011](#)). In mountainous regions in particular (e.g., the Southern Appalachian Mountains, SAM), where persistent fog and low-level clouds are strongly modulated by complex topography ([Duan and Barros, 2017](#); [Wilson and Barros, 2014, 2017](#)), severe cloud contamination can significantly handicap the use of optical remote sensing products. However, to date most efforts in the remote sensing community that have been devoted to improving the accuracy of remote sensing products tend to focus on assessments of land-use land-cover (LULC) change impacts ([Baret et al., 2013](#); [Camacho et al., 2013](#); [Liang et al., 2014](#); [Liu et al., 2013](#); [Masson et al., 2003](#); [Myneni et al., 2002](#); [Xiao et al., 2014](#)), and less so in systematically evaluating their fidelity in the context of the water cycle generally, and watershed hydrology in particular. Previous studies that investigated hydrological impacts of time-varying vegetation characteristics (e.g., [Ford and Quiring, 2013](#); [Tesemma et al., 2015](#); [Yildiz and Barros, 2007](#)) did not discuss the impacts of cloud contamination on the quality of remote sensing products. For instance, [Parr et al. \(2015\)](#) replaced climatologically-based LAI with dynamic LAI data directly using the MODIS standard product in the VIC model to improve the estimation of evapotranspiration and streamflow without discussing the quality control for the MODIS LAI product and its impact on VIC calibration. Likewise, the quality of AVHRR data were taken at face-value by [Yildiz and Barros \(2005, 2007 and 2009\)](#). Further, it is difficult to detect and attribute error to vegetation parameters in many modeling studies due to the short time span of simulations (e.g., days in [Kumar et al., 2014](#); 29 cloud-free days in [Long et al., 2011](#)). The cumulative long-term impacts of using high-quality (i.e., with cloud correction) time-variant vegetation characteristics products at high temporal resolution (e.g., at least daily to sub-daily) on basin-scale simulations of water fluxes (e.g., evapotranspiration, streamflow, etc.) remain to be investigated.

Similar challenges affect two other key land surface radiative parameters examined here: the shortwave broadband albedo and longwave broadband emissivity. Broadband emissivity is required for hydrological modeling to quantify emitted longwave radiation over the full electromagnetic spectrum (mainly longwave/thermal infrared, $\sim 8\text{--}12\ \mu\text{m}$), and broadband albedo is used to quantify the fraction of incoming shortwave radiation ($\sim 0.3\text{--}3\ \mu\text{m}$) that is reflected, which varies instantaneously with solar zenith angle and illumination geometry (Schaaf et al., 2002; Wang et al., 2004). These two radiative properties are also important indicators of land-cover change over long time-scales (e.g., deforestation and reforestation) (Dickinson and Kennedy, 1992; Dirmeyer and Shukla, 1994; Garratt, 1993; Liu, 2011; Qu et al., 2015), as well as indicators of land surface disturbances (e.g., wildfires), hydroclimate conditions (e.g., wet or drought), and irrigation practices at shorter time scales (Jin et al., 2012; Pryor et al., 2016), and thus vary both in space and time (especially the surface broadband albedo). However, there are no spatially and temporally varying surface shortwave broadband albedo and longwave broadband emissivity products available for direct use in hydrologic applications. For instance, MODIS products include daily or 16-day spectral reflectance under a given observation geometry, spectral-band and also broadband BRDF (Bidirectional Reflectance Distribution Function) parameters, black-sky albedo (directional hemispherical reflectance) at a given solar zenith angle (e.g., at local solar noon) and white-sky albedo (bihemispherical reflectance) for certain range of bands, but continuous/gap-free products of actual land surface broadband albedo (blue-sky albedo, a weighted average of black-sky albedo and white-sky albedo with dynamic weights depending on the fraction of diffuse skylight) including diurnal variations as needed in high-resolution energy flux modeling are not available. In addition, MODIS emissivity products only provide daily, 8-day, and monthly narrowband emissivity data. Note that previous research has shown that large biases in estimated longwave radiation based on the Planck function and the Stefan-Boltzmann law could be attributed to using spectral (narrowband) emissivity instead of broadband emissivity (Wang et al., 2005).

Although detailed algorithms for mapping surface broadband albedo using satellite-based BRDF parameters (Schaaf et al., 2002) and the narrowband-to-broadband conversion algorithms for generating surface broadband emissivity and albedo from spectral observations (Jin and Liang, 2006; Liang et al., 1999) have been widely used in the remote sensing community (Qu et al., 2015), the importance of this work has not been well recognized and transferred to the hydrological modeling community. Indeed, almost all currently used LSMs and hydrological models still adopt either land-cover-dependent static albedo estimated by radiative transfer models (e.g., the two-stream approximation described in Bonan, 1996; Zeng et al., 2002) or the spatially-varying but temporally semi-invariant (e.g., climatologically-based seasonal or diurnal varying) albedo derived from satellite observations (e.g., MODIS and AVHRR) (Csiszar and Gutman, 1999; Strugnell et al., 2001) that are characterized by improved accuracy relative to the former (Oleson et al., 2003; Wei et al., 2001). Using static or semi-static albedo influences the surface energy budget, the land-surface skin temperature, and thus the energy exchange at the air-ground interface. For instance, Cedilnik et al. (2012) found that using daily bihemispherical (white-sky) albedo derived from satellite BRDF parameters instead of climatologically-based monthly albedo in NWP (Numerical Weather Prediction) simulations significantly reduced the bias in modeled surface net radiation. Likewise, even very small changes in emissivity have a strong impact in the radiation budget when integrated over time because of the fourth power dependence of emitted longwave radiation on the surface temperature in the application of the Stefan-Boltzmann Law (see also Forster et al. (2007) for relevant climate sensitivity discussion).

To this end, the specific scientific questions we aim to address in this study include 1) what is the impact of incorporating corrected spatially and temporally varying landscape attributes (i.e., vegetation characteristics and surface radiative properties) into a distributed hydrological model on the simulations of streamflow and evapotranspiration; and 2) what is the quantitative impact of using corrected landscape attributes data on the hydrologic chain of interacting processes (rainfall – interception – evapotranspiration - soil moisture – runoff - streamflow, net longwave and shortwave radiation – net surface radiation – sensible heat flux – soil temperature, etc.), and consequently on the basin-integrated water and energy budgets in topographically complex regions. We hypothesized that (i) large uncertainty and errors are present within remote-sensing (specifically MODIS) standard products of landscape attributes especially over mountainous regions such as the SAM where persistent clouds and lingering heavy-fog handicap satellite-based data acquisition, and that such errors can be corrected at least in part by appropriate post-processing methods; (ii) vegetation attributes (LAI and FVC) strongly impact the simulations of evapotranspiration and streamflow both at short- and long-time scales; therefore, the corrected vegetation parameters should improve the simulations of streamflow and regional water budget; and (iii) using realistic temporally and spatially varying radiative properties (albedo and emissivity) will result in improved simulations of the diurnal cycle and sub-seasonal and seasonal variability of the surface energy budget including the net total radiation and sensible heat fluxes compared to using the conventional treatment to albedo and emissivity (i.e., land-cover-dependent values). To test these hypotheses, we first developed high-quality radiative and vegetation properties datasets from MODIS standard products (see Table 1) over the IPHEX2014 domain (Integrated Precipitation and Hydrology Experiment 2014, see Section 2 and Barros et al.

Table 1
Summary of the MODIS Products used in this project⁸.

Short name	Platform	MODIS Product	Raster type	Resolution	Temporal Granularity
MCD15A2	Combined	Leaf Area Index - FPAR	ISG Tile	1000 m	8 day
MOD11C2	Terra	Land Surface Temperature & Emissivity	CMG	5600 m	8 day
MCD43B1	Combined	BRDF-Albedo Model Parameters	ISG Tile	1000 m	8day (16 days acquisition interval)
MCD12Q1	Combined	Land Cover Type	ISG Tile	500 m	Yearly
MOD08_D3	Terra	Atmosphere Daily Global Product	Gridded	1degree	Daily

⁸ISG: Integerized Sinusoidal Grid; CMG: Climate Modeling Grid.

(2014)) in the southeast (SE) US at a spatial resolution of $1\text{ km} \times 1\text{ km}$ and hourly time step continuously for a seven-year time period 2007–2013. These data-sets were used for operational hydrological forecasting during IPHEX using the fully distributed Duke Coupled surface-subsurface Hydrology Model (DCHM, Tao et al., 2016). Here, five modeling experiments were designed to systematically evaluate the propagation of errors associated with standard MODIS products on DCHM simulations of water and energy fluxes in three headwater basins, and to characterize the integrated impact of using the improved landscape attributes on basin-scale water and energy budgets.

The objective of this study is two-fold: (i) to present a straightforward framework for systematically developing high-quality time-varying vegetation characteristics and radiative properties that reflect realistic land surface variability (e.g., land-cover-land-use change caused by both natural and human-activity factors) for hydrologic applications in regions of complex terrain for the first time at hourly temporal-resolution; and then, (ii) to examine both the long-term (years) and short-term (one-month) impacts of using these realistic dynamic (i.e., high-quality spatially and temporally varying) landscape attributes on water and energy budgets at basin scale using the DCHM. Throughout the paper, the term “landscape attributes” refers to both “surface radiative properties” and “vegetation parameters”, where the “surface radiative properties” specifically refer to longwave broadband emissivity and shortwave broadband albedo, and the “vegetation parameters” refer to LAI and FVC. The developed data over the IPHEX domain in the SE US are publicly and freely available at Duke University (DOIs and links are provided at the end of this article). Moreover, the framework presented here provides an easy-to-follow roadmap for hydrologists to generate quality and continuous/gap-free data for their modeling studies in different regions or different periods of interest.

The study region and IPHEX2014 are described in Section 2. The hydrological model, the methodology for deriving high-quality hourly surface radiative properties and vegetation characteristics products, as well as the experimental design to examine the research hypotheses enunciated above are described in Section 3. Section 4 presents the newly developed datasets focusing on the improvement with respect to MODIS standard products without post-processing. The value of the new datasets to improve the fidelity of multi-year hydrologic simulations is assessed in Section 4, along with an illustrative process analysis of simulated water and energy fluxes using a limited duration case-study (one-month). Section 5 provides a summary of the work and further discussion.

2. Study area and evaluation data

The IPHEX2014 was a Ground Validation (GV) field campaign in support of NASA's Global Precipitation Measurement (GPM) satellite mission (Barros et al., 2014; Petersen and Barros, 2018). The IPHEX domain is centered on the Southern Appalachian Mountains (SAM) and spans the Piedmont and Coastal Plain regions of the SE US, centered on the four river basins with headwaters in the Southern Appalachians: Upper Tennessee River Basin, Savannah River Basin, Santee River Basin and Yadkin-Pee Dee River Basin, as shown in Fig. 1. A key objective of IPHEX was to improve Quantitative Precipitation Estimates (QPEs) and Quantitative Precipitation Forecasts (QPFs) with application to hydrologic forecasting activities in regions of topographically complex terrain (e.g., the inner regions of the SAM). Under the auspices of IPHEX, an operational hydrological forecasting testbed was established during the intensive observing period (IPHEX-IOP) for 12 headwater basins in the inner region of SAM (Tao et al., 2016). In preparation for

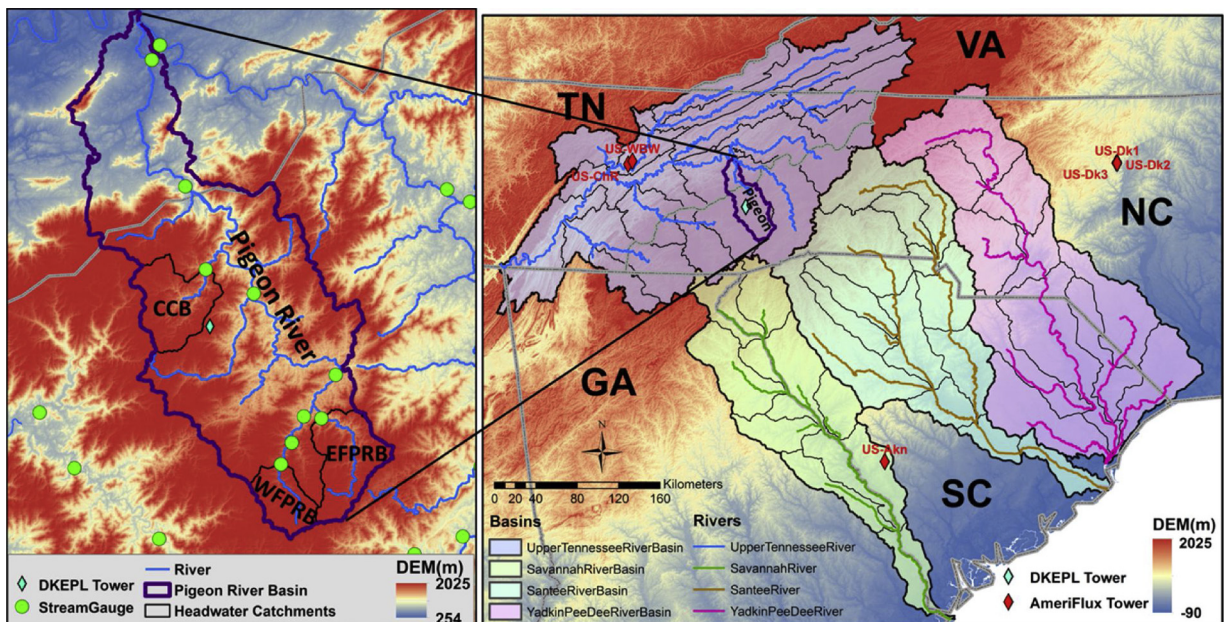


Fig. 1. Left panel: Pigeon River Basin (PRB). The hydrological verification will be conducted for three sub-basins that are not limited by dam operations in the PRB: the Cataloochee Creek Basin (CCB), the West Fork Pigeon River Basin (WFPRB) and the East Fork Pigeon River Basin (EFPRB). Right panel: IPHEX2014 domain and location of Ameriflux and Duke towers.

Table 2

Land cover at the Ameriflux tower locations.

Station	Lat.	Lon.	Elev.(m)	MODIS Land cover (IGBP)	MODIS Land cover (UMD Type)	Tower footprint
US-ChR	35.9311	-84.3324	286	Deciduous Broad-leaf Forest	Deciduous Broad-leaf Forest	Chestnut ridge
US-Dk1	35.9712	-79.0934	168	Mixed Forest	Woody Savannas	Grassland, open field
DKEPL Tower	35.5877	-83.0647	1486	Mixed Forest	Mixed Forest	Forest

the forecasting testbed, a benchmark project for generating high-quality, consistent data sets necessary (including hydro-geographic data, soil hydraulic parameters, atmospheric forcing, landscape attributes, etc.) to implement and operate hydrologic models for the major river basins in the SE US was completed for a 7-year period (2007–2013). Using high-quality historical atmospheric forcing (Tao and Barros, 2018) and the landscape attributes data presented here and described in the data report (Tao and Barros, 2014b), it was possible to conduct long-term hydrological model spin-up simulations to generate realistic initial conditions (e.g., soil moisture and water tables) for operational hydrological forecasting during the IPHEx-IOP (Tao et al., 2016) and evaluate the QPEs and QPFs products driving the DCHM.

Previously, point evaluation of the developed atmospheric forcing fields was conducted at four Ameriflux towers and the Duke Environmental Physics Laboratory (DKEPL) tower at Purchase Knob in the SAM (marked in Fig. 1) (Tao and Barros, 2018). The Ameriflux towers monitor key variables/states affecting ecosystem carbon, water, and energy fluxes, including atmospheric pressure, atmospheric temperature, upwelling and downward longwave radiation and shortwave radiation. Albedo can be estimated from the reflected global solar radiation divided by the incoming global solar radiation observations. However, the comparison of tower observations with the constructed albedo at 1 km resolution is limited by the spatial heterogeneity and the uncertainty associated with the spatial scale gap (e.g., from the point scale to pixel scale), that is its representativeness (Cescatti et al., 2012; Liu et al., 2009; Román et al., 2011, 2013; Román et al., 2009). To assess whether the tower-based albedo estimates can represent the spatial variability of the surrounding landscape at the spatial scales of MODIS products, Román et al. (2009) concluded in their study that the US-ChR tower (Fig. 1 and Table 2) is the only tower spatially representative of its surrounding landscape in the SE US. Thus, the albedo measurements at US-ChR are used here to validate our constructed albedo estimates from MODIS BRDF parameters.

Although there are no available observations of LAI, FVC and emissivity at the AmeriFlux towers, the newly developed data are contrasted against standard MODIS products at three selected flux tower locations with different land-cover types and very distinct topography (Table 2). In addition, an indirect evaluation strategy was pursued through end-to-end hydrologic modeling to examine the fidelity of the developed landscape attributes data by comparing simulated streamflow against observations. Specifically, three headwater catchments of the Pigeon River Basin (PRB) in the SAM that are equipped with USGS (United States Geological Survey) stream gauges but not affected by dam operations were selected to evaluate the hydrological simulation results: the Cataloochee Creek Basin in the inner mountain region (CCB, 128 km²), and the West Fork Pigeon River Basin (WFPRB, 71 km²) and the East Fork Pigeon River Basin (EFPRB, 131 km²) on the eastern ridges of the SAM (Fig. 1). The PRB features topographically complex terrain, characterized by gentle to very steep slopes and dominated by very dense forest (mix forest and deciduous broadleaf forest, Figure S1 in the supplementary file). The three headwater basins exhibit very different hydro-geomorphic features: the WFPRB has relatively shallower soils and limited aquifer storage, while the CCB and EFPRB have deep alluvial deposits with large subsurface flow (Tao and Barros, 2013 and 2014a). Besides, the CCB is at the lowest elevation among the three basins, and WFPRB and EFPRB sit at the highest elevation nested among the eastern ridgelines of the SAM. Notably, the hydrometeorology of the CCB is characterized by a strong diurnal cycle with persistent low-level clouds, fog, and light rainfall in the inner valleys in addition to persistent cloudiness above the ridges for all three basins at midday consistent with the time of satellite overpass (e.g., Duan and Barros, 2017; Wilson and Barros, 2014). Therefore, the original MODIS standard products are expected to have the lowest quality over CCB among the three basins, and the larger hydrologic impacts should also be expected in simulations of CCB hydrology.

3. Methodology

3.1. Duke coupled surface-groundwater hydrology model (DCHM) and the input data

3.1.1. Brief introduction to DCHM

The DCHM (Duke Coupled surface-subsurface Hydrology Model) has evolved over the years from a column SVAT (Soil-Vegetation-Atmosphere) implementation (Devonec and Barros, 2002) with dynamic vegetation (Garcia-Quijano and Barros, 2005) to a fully distributed hydrologic model (Yildiz and Barros, 2005, 2007 and 2009) including progressively more detailed representation of surface-groundwater interactions and flood propagation at a very high tempo-spatial resolution (e.g., 250 m and 5 min in Tao and Barros, 2013 and 2014a; Tao et al., 2016). The components/processes in the DCHM that are relevant to the developed data sets are described in the Appendix A more detailed description can be found in Tao (2015). The equations/processes directly or indirectly influenced by the landscape attributes prescribed in the DCHM are synthesized in Table 3.

The emissivity and albedo not only directly affect net longwave, net shortwave, and thus net total radiation, but also the surface latent and sensible heat fluxes as indicated by Table 3 and Equation (AP1) in the Appendix. Specifically, Equation (AP3) describes how albedo controls the magnitude of reflected solar radiation, and thus affects the total net solar/shortwave radiation, while emissivity affects the outgoing/longwave radiation; together both directly impact the total net radiation (Eq. (AP3)) which in turn

Table 3

Hydrological processes and the corresponding DCHM equations included in Appendix that are directly or indirectly influenced by the input landscape attributes data.

Variables	Equations	Directly Influenced Process	Indirectly Influenced Process
LAI	(AP3) ~ (AP11)	Interception, Evapotranspiration (bare soil evaporation, canopy skin evaporation and transpiration)	Infiltration, latent heat flux, overland flow (runoff), subsurface flow, streamflow, etc.
FVC	(AP3) ~ (AP11)	Interception, Evapotranspiration (bare soil evaporation, canopy skin evaporation and transpiration)	Infiltration, latent heat flux, overland flow (runoff), subsurface flow, streamflow, etc.
Albedo	(AP1) ~ (AP4)	Outgoing/reflected shortwave radiation, net shortwave radiation	Total net radiation, sensible heat flux, soil temperature, ground heat flux, etc.
Emissivity	(AP1) ~ (AP4)	Outgoing/emitting longwave radiation, net longwave radiation,	Total net radiation, sensible heat flux, soil temperature, ground heat flux, etc.

affects the surface energy budget, soil temperature, and sensible, latent, and ground heat fluxes (Eq.(AP1)). The LAI and FVC modulate rainfall interception, evapotranspiration, and thus soil moisture and streamflow response. LAI directly influences the calculation of canopy resistance (Jarvis formulation, Eq. (AP8)) and thus significantly impacts the estimations of transpiration (AP7). Besides, it is also used for determining the storage capacity of the canopy skin reservoir (and thus affects canopy skin evaporation) and the interception capacity (and thus controls rainfall interception; as per Eq. (AP11), that is rainfall partitioning. The FVC (i.e., the fractional vegetation coverage) represents the ratio of the vegetated area within a grid cell to the total area of the grid, and it modulates evapotranspiration by weighting the magnitude of canopy skin evaporation, vegetation transpiration, and bare soil evaporation (Eq. AP6). Note that the energy balance equations (Eq. AP1) and water balance equation (Eq. AP9) are fully coupled in the DCHM relying on a semi-implicit numerical scheme (e.g., Crank-Nicholson scheme following Devonec and Barros (2002)). Thus, the changes in water fluxes caused by the vegetation attributes also influence the energy partitioning, and the impacts of radiative properties on energy fluxes feedback into the water fluxes. Nevertheless, relative to the impacts on water fluxes caused by vegetation attributes, the influence of radiative properties on water fluxes is comparatively small.

The DCHM has been used in previous hydrological studies in headwater basins of PRB (see Section 2) to investigate the predictability of flash floods and debris flow initiation for particular (short-term) storm events (Tao and Barros, 2013, 2014a; Tao et al., 2016). Here, the focus is on sensitivity analysis of long-term hydrological simulations and thus the time-integrated impacts of landscape attributes data. We conducted all DCHM simulations at the IPHEx nominal resolution (1 km × 1 km and hourly time-step) (see details about model simulation configurations in Section 3.3).

3.1.2. Input data required by DCHM

The DCHM (and distributed hydrological models generally) require two types of input - the generic static (time-invariant) parameters and dynamic (time-variant) inputs including meteorological forcing and landscape attributes. All the input data have to be consistently prepared at a unified spatiotemporal resolution under the same projected coordinate system (i.e., UTM17 N at WGS84 datum in this study). Note the spatial resolution and temporal resolution has to be closely related to assure computational stability of numerical modeling. For the IPHEx nominal spatial resolution at 1 km × 1 km, an hourly temporal resolution is adequate to ensure numerical stability.

3.1.2.1. Static (time-invariant) parameters. The most fundamental hydro-geographical static dataset required by DCHM, the Digital Elevation Model (DEM) data were extracted from the Shuttle Radar Topography Mission (SRTM) data (Farr et al., 2007) from which DCHM calculates slopes and flow directions at model grid pixels. Soil hydraulic parameters (including saturated hydraulic conductivity, porosity, field capacity, and wilting point) were extracted from the State Soil Geographic (STATSGO) dataset (Miller and White, 1998). Also, we extracted land-cover data over the IPHEx domain from the MODIS Terra and Aqua combined Land Cover Type Yearly Global product at ~500 m (463.3 m) resolution (MCD12Q1, V051) and generated yearly land-cover for IPHEx at 1 km spatial resolution. Although mixed land-cover types may be present, it is assumed that the physical processes are dominated by the majority of the land-cover type in each pixel.² The resultant land-cover data in 2009 for the Pigeon River Basin as well as over the SE US in 2009 are shown in Figure S1 (in the supplementary file) as an example with a GoogleEarth™ image included for reference. The landcover product is subsequently used in DCHM to specify temporally-invariant, spatially-distributed physical vegetation parameters including the minimum stomatal resistance, roughness length and displacement height (thus affecting the calculation of aerodynamic drag coefficients) (Dickinson et al., 1993; Mahfouf et al., 1995), as well as the vertical distribution of vegetation root (Zeng, 2001). All these static data are publicly available from the IPHEx website³.

3.1.2.2. Dynamic (time-variant) input - meteorological forcing fields. Precipitation input to DCHM, as the most important meteorological forcing, was generated from the National Center for Environmental Prediction (NCEP) Stage IV data, a mosaic precipitation analyses product derived from multi-sensor (Next Generation Weather Radar and rain-gauges) over the US (Baldwin and Mitchell, 1998; Lin and Mitchell, 2005). We first downscaled the Stage IV data from 4 km to 1 km using a transient multifractal

² <http://iphex.pratt.duke.edu/DataCenter/Time-invariantDatasets/LandCover>

³ <https://iphex.pratt.duke.edu/DataCenter/Time-Invariant%20Datasets>

downscaling method (Nogueira and Barros, 2015), and then used the ensemble mean of 50 hourly downscaled rainfall fields for the hydrological simulations presented here. Other atmospheric forcing fields (e.g., air temperature, air pressure, specific humidity, wind speed, incoming shortwave and longwave radiation) were downscaled from the 32-km 3-hourly North American Regional Reanalysis (NARR) data to the IPHEx nominal resolution (i.e., 1 km × 1 km and hourly time-step), and were physically corrected for elevation, topography and cloudiness effects as described in the companion paper (Tao and Barros, 2018). The developed atmospheric forcing fields are publicly and freely available at Duke Library⁴ (DOI: 10.7924/G8RN35S6).

3.1.2.3. Dynamic (time-variant) input - landscape attributes. The landscape attributes data specifically include LAI, FVC, surface longwave broadband emissivity and shortwave broadband albedo. As elaborated in the introduction, current MODIS standard LAI products have large severe errors caused by persistent cloud or cloud/fog contamination. Also, there are no standard longwave broadband emissivity and shortwave broadband albedo products. Here, we develop continuous quality LAI data by adjusting and then correcting cloud impacts within the MODIS LAI product (Section 3.2), and then calculate FVC with the corrected LAI data. For emissivity, we use a narrowband-to-broadband method (Section 3.2) to calculate the longwave broadband emissivity with the MODIS standard narrowband emissivity products first and then adjust the estimates further to correct potential errors. Regarding albedo, we construct hourly shortwave broadband albedo with MODIS BRDF broadband parameters (see details in Section 3.2.3). The new landscape attributes data with correction are publicly and freely available from Duke Library⁵ (DOI: 10.7924/G8H41PBG).

3.2. Developing high-quality vegetation parameters and surface radiative properties for distributed hydrologic modeling

We developed continuous radiative properties (i.e., emissivity and albedo) and vegetation parameters (i.e., LAI and FVC) over the SE US at the IPHEx nominal resolution (1 km × 1 km and hourly time-step) for seven years (2007–2013). Fig. 2 illustrates the workflow including the data-model links (i.e., how the landscape attributes data are used in the DCHM) as described in detail in Section 3.1.1 and the Appendix. The detailed description of the methodology implemented to produce the high-quality landscape attributes data are presented in the technical report by Tao and Barros (2014b). Here, we describe the core methodology and algorithms only.

The focus is specifically on the correction of cloud/fog contamination within MODIS land products (listed in Table 1) using temporal filtering method. Before any post-processing, the relevant standard MODIS products were first re-projected to UTM17 N (WGS84), composited to the study area, and then interpolated to the IPHEx domain grid system at 1 km × 1 km resolution. Subsequently, physically-based checks (e.g., seamless composition, artifacts, etc.) and temporal filtering were conducted to correct cloud and fog contamination toward reducing discontinuities and abnormal values in LAI, FVC, and emissivity. Finally, linear interpolation was applied to generate hourly products for the corrected vegetation data and emissivity. As illustrated by Fig. 2a, hourly albedo was constructed mainly relying on MODIS BRDF parameters, which differs from the methods applied for generating hourly emissivity, LAI, and FVC.

3.2.1. Vegetation parameters: LAI and FVC

The standard LAI data were extracted from the combined Terra and Aqua MODIS 8-day LAI product (MCD15A2, Collection 5). The MCD15A2 LAI product was retrieved based on a look-up-table that represents the LAI-FPAR-reflectance relationship estimated by a three-dimensional radiative transfer model (Mynden et al., 2002). Here, we follow the method presented in Yuan et al. (2011) to improve MODIS LAI to remove cloud impacts.

The core data processing algorithm is TIMESAT, a tool utilized for analyzing time-series data has been widely applied for post-processing satellite products (Eklundh et al., 2009; Heumann et al., 2007; Yuan et al., 2011). The adaptive Savitzky-Golay filter in TIMESAT that fits the input time-series data using a quadratic polynomial function was used to conduct the adaptive temporal filtering for MODIS products. The method detects spikes/outliers and assigns weights to the LAI data relying on the Seasonal Trend Decomposition using Loess (STL) algorithm, which first decomposes the time series into trends, seasonality and remainder components and then assigns the weights accordingly. Important TIMESAT parameters, including the weights, moving window size of polynomial fit, and strength of the envelope adaptation, etc., were carefully investigated through sensitivity analysis. In general, high weights are assigned to good quality data (e.g., clear-sky conditions) and low weights for the data with bad quality control flags (e.g., cloudy conditions). The moving window size (8) for the Savitzky-Golay filter was determined iteratively to achieve the best fit to the upper envelope of the data and avoid negative bias. Other parameters were assigned according to the discussion and suggestions in the software manual by Eklundh and Jönssonb (2012).

As indicated in Fig. 2a, TIMESAT was applied first to filter LAI temporally, and the gap-free LAI data were used to calculate FVC based on an empirical relationship (Choudhury, 1987; Choudhury et al., 1994; French et al., 2003a; Steven et al., 1986):

$$FVC = 1 - \exp(-K \times LAI) \quad (1)$$

where $\exp(-K \times LAI)$ represents the canopy transmittance, and K is the attenuation coefficient, or, a leaf angle distribution term which is defined as 0.5 for the case of randomly oriented leaves (Choudhury et al., 1994; French et al., 2003b; Ross, 1975).

⁴ <http://dukespace.lib.duke.edu/dspace/handle/10161/8958>

⁵ <http://dukespace.lib.duke.edu/dspace/handle/10161/8968>

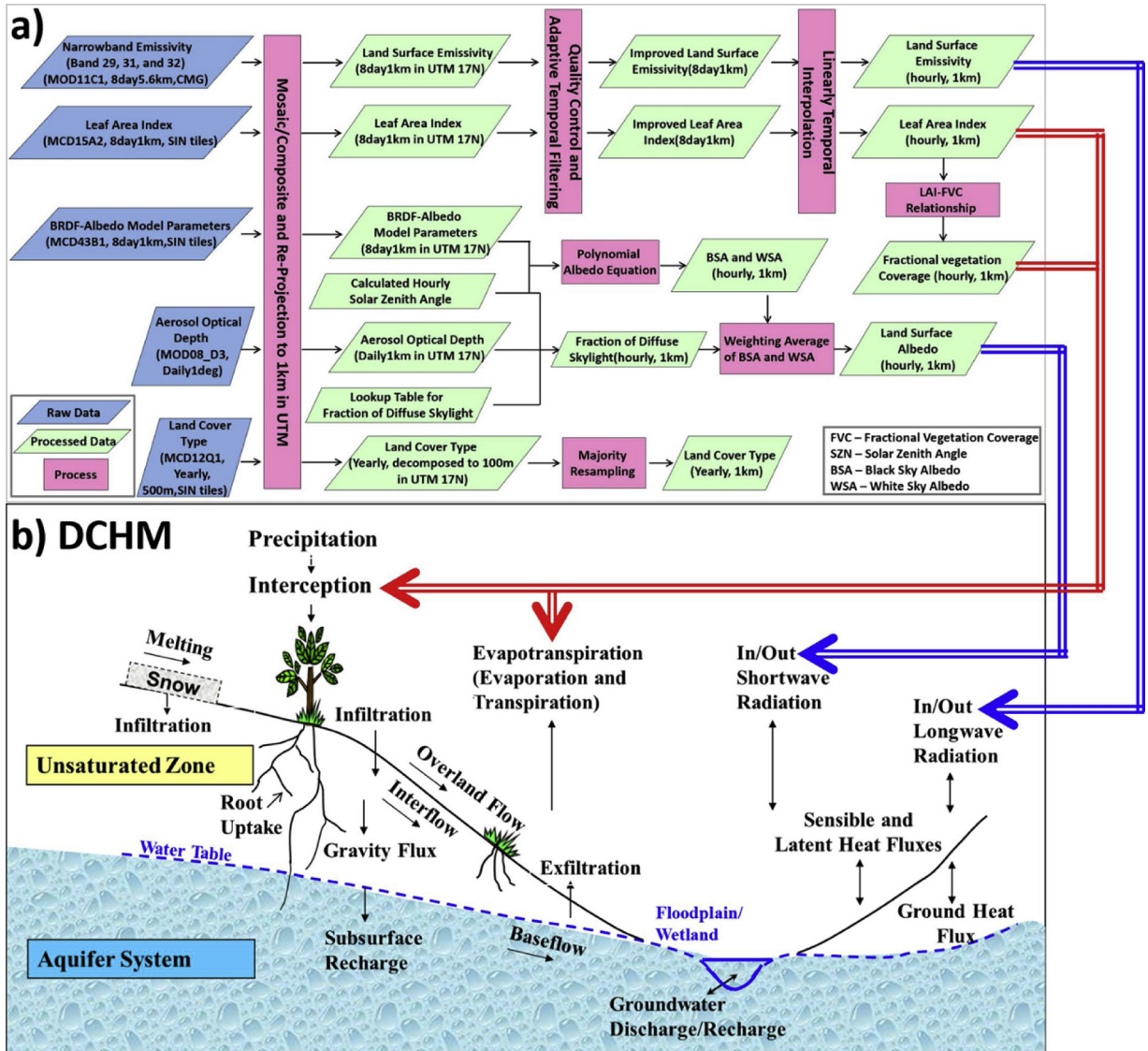


Fig. 2. a) Flowchart for generating quality landscape attributes datasets, including land surface shortwave broadband albedo, land surface longwave broadband emissivity, LAI and FVC from MODIS products, which are then used in the DCHM of which the conceptual modeling framework is shown in b) with link functions connecting the landscape attributes data and the relevant hydrologic processes.

3.2.2. Land surface longwave broadband emissivity

The MODIS/Terra 8-Day Land Surface Temperature and Emissivity product on a latitude/longitude-based (0.05°) climate modeling grid system (MOD11C2, Collection 5) consists of spectral emissivity for the various MODIS bands. A linear relationship between the MODIS broadband emissivity and narrowband emissivity was established through regression analysis by Jin and Liang (2006), using the spectral emissivity at MODIS band 29 (ε_{29} , $8.400\text{--}8.700\mu\text{m}$), band 31(ε_{31} , $10.780\text{--}11.280\mu\text{m}$) and band 32 (ε_{32} , $11.770\text{--}12.270\mu\text{m}$) as follows:

$$\varepsilon_b = 0.0139 \times \varepsilon_{29} + 0.4606 \times \varepsilon_{31} + 0.5256 \times \varepsilon_{32} \quad (2)$$

This empirical relationship accounts for soil texture and mineral composition with the uncertainty of ± 0.005 (Jin and Liang, 2006). The broadband emissivity was calculated using Equation (2) first, followed by temporal filtering using TIMESAT (Fig. 2a). As opposed to the STL-decomposition method used for LAI data, sensitivity analysis demonstrated that the median filtering method was the most efficient approach to detect emissivity outliers, resulting in very similar weights as the STL-decomposition method. Thus, the median filtering was selected for detecting spikes in the emissivity data, while other parameters were derived using the same approach as for the LAI data (e.g., fitting method is Savitzky-Golay, seasonality parameter, etc.). Because emissivity data are governed by landcover, soil moisture content and vegetation characteristics, the upper envelope is not necessarily the true value. The STL-decomposition method is more favorable for fitting to the upper envelope of data, such as in the case of LAI.

3.2.3. Land surface shortwave broadband albedo

Currently, there is no available standard albedo product at high temporal resolution (i.e., hourly) because it depends on the instantaneous solar zenith angle and illumination geometry at local-scales (Liu et al., 2009; Schaaf et al., 2002). Here, the MODIS BRDF/Albedo Model Parameters product (MCD43B1) that provides both spectral-band and broadband BRDF (Bidirectional Reflectance Distribution Function) model parameters every 8 days (with 16 days acquisition interval) was used to construct time-varying albedo as a function of solar zenith angle and solar illumination geometry following Schaaf et al. (2002). Given that the MCD43B1 was produced with 16 days acquisition intervals with fewer gaps compared to vegetation products, we do not apply post-processing to this product and use it to construct the surface albedo directly (Fig. 2a).

The new hourly albedo product developed here is a function of the black-sky albedo (BSA, or directional hemispherical albedo) and white-sky albedo (WSA, or bihemispherical albedo). Relying on the Ross-Thick/Li-Sparse-Reciprocal (RTLSR) kernel-driven BRDF model, the BSA ($\alpha_{bs}(\theta, \lambda)$) for any solar illumination geometry is derived by calculating the weighted sum of an isotropic parameter and kernels describing viewing and illumination geometry (Román et al., 2009; Schaaf et al., 2002) as follows:

$$\begin{aligned}\alpha_{bs}(\theta, \lambda) = & \sum_k f_k(\lambda)(g_{0k} + g_{1k}\theta^2 + g_{2k}\theta^3) = f_{iso}(\lambda)(g_{0iso} + g_{1iso}\theta^2 + g_{2iso}\theta^3) + f_{vol}(\lambda)(g_{0vol} + g_{1vol}\theta^2 + g_{2vol}\theta^3) \\ & + f_{geo}(\lambda)(g_{0geo} + g_{1geo}\theta^2 + g_{2geo}\theta^3)\end{aligned}\quad (3)$$

where λ indicates a waveband (e.g., either spectral band or band ranges) and here specifically means the shortwave broadband (0.3–3 μm); θ is the solar zenith angle; g_{jk} ($j = 0, 1$, and 2, and $k \in (iso, vol, geo)$) are the coefficients provided in Schaaf et al. (2002); $f_{iso}(\lambda)$ is the isotropic scattering component, $f_{vol}(\lambda)$ is the parameter for the Ross-Thick volume scattering kernel, and $f_{geo}(\lambda)$ is the parameter for the Li-Sparse-Reciprocal geometric scattering kernel. These BRDF model parameters including $f_{iso}(\lambda)$, $f_{vol}(\lambda)$, and $f_{geo}(\lambda)$ are provided in the MCD43B1 8-day products. Note we only use the shortwave broadband (0.3–3 μm) BRDF parameters within MCD43B1 products to construct the hourly shortwave broadband albedo.

The WSA ($\alpha_{ws}(\lambda)$) can be directly calculated using these BRDF parameters and the following empirical Eq. (4):

$$\alpha_{ws}(\lambda) = f_{iso}(\lambda) + 0.189184f_{vol}(\lambda) - 1.377622f_{geo}(\lambda) \quad (4)$$

It is important to emphasize that the WSA ($\alpha_{ws}(\lambda)$) relies on the MCD43B1 BRDF parameters, and thus it is assumed constant over the 8-day period of the MCD43B1 product. The BSA ($\alpha_{bs}(\theta, \lambda)$), in contrast, is calculated at hourly time steps with the specific solar zenith angle at each pixel albeit using the same BRDF parameters over the 8-day period.

Finally, the actual (blue-sky) albedo $\alpha(\theta, \lambda)$ of the land surface is the weighted average of $\alpha_{bs}(\theta, \lambda)$ and $\alpha_{ws}(\lambda)$, where the weighting coefficient is the fraction of diffuse skylight $S(\theta, \tau(\lambda))$:

$$\alpha(\theta, \lambda) = [1 - S(\theta, \tau(\lambda))] \alpha_{bs}(\theta, \lambda) + S(\theta, \tau(\lambda)) \alpha_{ws}(\lambda) \quad (5)$$

The $S(\theta, \tau(\lambda))$ was obtained from a lookup table⁶ relating solar zenith angle θ , atmospheric optical depth $\tau(\lambda)$ and local aerosol types to diffuse skylight (Schaaf et al., 2002). The aerosol optical depth, a measurement of the extinction of solar radiation through the atmosphere due to absorbing or scattering by aerosol particles, was obtained from the MODIS Level 3 Atmosphere Daily Product (MOD08_D3). The actual albedo $\alpha(\theta, \lambda)$ at hourly time-scale was calculated by Eq. (5) with hourly $S(\theta, \tau(\lambda))$ and hourly $\alpha_{bs}(\theta, \lambda)$ assuming that $\alpha_{ws}(\lambda)$ does not change over the 8-day period consistent with the MCD43B1 product.

3.3. Hydrologic simulations

To investigate the hydrological impacts of the land attributes and demonstrate the value and utility of the corrected time-varying landscape attributes datasets, hydrological simulations at the IPHEx nominal resolution (1 km × 1 km and hourly time-step) were conducted using DCHM in three headwater sub-basins of the Pigeon River Basin in the Southern Appalachian Mountains (see Section 2) for four continuous water years from 2007 October to 2011 September encompassing an extreme drought (2007–2008) and a very wet hydrological year (2009–2010) (Brun and Barros, 2013).

3.3.1. Hydrologic simulation experiments design

To examine the 2nd and 3rd hypotheses of the study, we designed five modeling experiments as described in Table 4 that includes the list of the subset of figures with results relevant for each experiment. Throughout the paper, “standard” refers to MODIS standard products without any post-processing (i.e., correction/adjustment). Specifically, the standard LAI was directly extracted from MODIS MCD15A2 product (Section 3.2.1) without any correction, and the standard FVC was calculated using the standard LAI. In summary, the terminology “standard vegetation attributes” refers to standard LAI and FVC, and the terminology “adjusted vegetation attributes” refers to corrected LAI and the estimated FVC based on the corrected LAI as described in Section 3.2.1.

Regarding surface radiative properties, since albedo and emissivity together impact the net total radiation in the energy balance equation (AP1) that further affects hydrological processes along the heat exchange chain, the two variables were examined in three categories: conventional treatment, standard treatment, and constructed temporally and spatially varying data (Table 4). The conventional treatment of radiative properties follows the approach used in the Noah model (Kumar et al., 2011) by assigning static values for albedo and emissivity according to land-cover type (i.e., LC-dependent) as provided in Table 5. There are no “standard”

⁶ <http://www-modis.bu.edu/brdf/userguide/tools.html>

Table 4

Hydrologic simulation experiments conducted in the study.

Simulations	Vegetation Characteristics (LAI& FVC [§])	Radiative Properties (Albedo [*] and Emissivity [#])	Figures
Experiment1 (Exp1)	Adjusted	Constructed: Constructed albedo; Adjusted emissivity.	Figs. 8–12
Experiment2 (Exp2)	Standard	Standard Treatment: LC-dependent albedo; Standard emissivity.	Fig. 8
Experiment3 (Exp3)	Standard	Constructed: Constructed albedo; Adjusted emissivity.	Figs. 9 and 10
Experiment4 (Exp4)	Adjusted	Conventional Treatment: LC-dependent albedo; LC-dependent emissivity	Figs. 11 and 12
Experiment5 (Exp5)	Adjusted	Standard Treatment: LC- dependent albedo; Standard emissivity.	Figure S4 in the supplementary file & Fig. 12

[§] Standard: Hourly LAI&FVC directly interpolated from MODIS standard LAI product; Adjusted: Hourly LAI&FVC interpolated from LAI corrected for cloudiness impacts (after temporal filtering).

* Constructed albedo: Hourly land surface shortwave broadband albedo produced by the authors in the context of the work described in Section 3.2.3. LC-dependent albedo: Static albedo assigned to each land cover type (as listed in Table 6).

[#] Standard emissivity: Hourly emissivity directly interpolated from the broadband data calculated using the MODIS standard narrowband emissivity product; Adjusted emissivity: Hourly emissivity interpolated from the calculated broadband emissivity after temporal filtering; LC-dependent emissivity: Static emissivity assigned to each land cover type (as listed in Table 6).

Table 5

Conventional treatment for land surface radiative properties (shortwave broadband albedo and longwave broadband emissivity): albedo and emissivity is assigned as static value according to each land cover type.

Land cover	Albedo	Emissivity
Evergreen needle leaf forests	0.12	0.95
Evergreen broadleaf forests	0.12	0.95
Deciduous needle leaf forests	0.14	0.935
Deciduous broadleaf forests	0.16	0.93
Mixed forests	0.17	0.95
Closed shrublands	0.25	0.93
Open shrublands	0.22	0.94
Woody savannas	0.25	0.93
Savannas	0.20	0.92
Grassland	0.19	0.94
Cropland	0.17	0.9525
Urban	0.15	0.88
Barren	0.38	0.90

shortwave broadband albedo and longwave broadband emissivity products. Here we define the standard emissivity as the longwave broadband emissivity directly calculated from MODIS narrowband emissivity using the same method as described in Section 3.2.2 (thus, it is also spatiotemporally-varying) but without corrections or adjustments. Therefore, the standard radiative properties include the standard emissivity and LC-dependent albedo. Finally, the constructed radiative properties refer to the datasets developed in this work including the spatiotemporally-varying emissivity with post-processing/adjustment (Section 3.2.2) and the constructed space-time variant albedo reflecting realistic surface conditions, atmospheric and environmental conditions, and solar illumination geometry based on MODIS shortwave broadband BRDF parameters (Section 3.2.3).

As indicated in Table 4, Exp1 uses the most realistic landscape attributes data including the adjusted vegetation attributes (i.e., LAI and FVC) and constructed temporally and spatially varying radiative properties (e.g., emissivity and albedo) produced in this study, and thus is the reference or benchmark for all sensitivity experiments. Exp2 uses the standard vegetation attributes and the standard treatment for radiative properties, representing the current standard configuration in hydrologic modeling practice with regard to the specification of land-surface radiative properties. The differences in simulated streamflow between Exp1 and Exp2 illustrate the integral impact of using more realistic vegetation attributes and radiative properties compared to using standard data, or in other words, the impact of the cloudiness correction applied to vegetation attributes and emissivity in addition to using the newly constructed spatiotemporally-varying albedo.

As described in Section 3.1.1, radiative properties mainly affect the simulations of energy fluxes and long-term energy budget, and vegetation characteristics primarily influence the simulations of water fluxes and long-term water budget. Thus, we also discuss the hydrological impacts of vegetation attributes and radiative properties separately. To examine the impacts of vegetation attributes alone on the simulations of water fluxes, Exp3 is designed to use the newly constructed radiative properties as in Exp1 and the standard vegetation attributes without correction. Comparing simulated water fluxes between Exp1 and Exp3 both at long- and short-time scales illuminates the propagation of errors from standard MODIS vegetation products in the hydrologic model and the translation of input errors into simulation bias. To examine the impacts of radiative properties alone on the simulations of energy fluxes, Exp4 uses the adjusted vegetation attributes as in Exp1, while prescribing the radiative properties with conventional treatment

(i.e., LC-dependent albedo and emissivity). We expect large diurnal and seasonal differences in the simulated energy fluxes between Exp1 and Exp4 given the contrasting differences between constructed radiative properties and the LC-dependent values. Finally, Exp5 differs from Exp4 only in the usage of standard emissivity. Comparing the differences between Exp1 and Exp4 with the differences between Exp 1 and Exp5 provides an alternative path for characterizing the value of using spatiotemporally-varying emissivity directly estimated from MODIS standard products relative to the conventional LC-dependent emissivity.

3.3.2. Analysis strategy

3.3.2.1. Long-term impacts. Errors and uncertainty in the initial soil water and groundwater storage severely impact streamflow predictability at the event scale by affecting the space-time structure of rainfall-runoff response across the watershed, as well as long-term water budgets in the case of continuous simulations. Thus, spin-up simulations similar to Tao and Barros (2018) and Tao et al. (2016) were conducted to redress uncertainty in initial conditions in all experiments in Table 4. Spin-up simulations are repeated simulation cycles using the same forcing for a period of time, with initial soil moisture and water table conditions equal to their values at the end of the preceding iteration until the differences between initial and end states are below a tolerance level. Note that, unless the atmospheric forcing is precisely known, the model structure is correct, and model parameters are accurate, it is not possible to completely eliminate uncertainty in the model initial conditions. The purpose of model initialization by spin-up is to achieve internal consistency among the unsaturated and saturated water stores in the model in synergy with the prevailing hydrometeorological regimes and regional conditions as described by the available atmospheric forcing, topography and land cover attributes.

Specifically, the four-year simulations were repeated 10 times, for a total of 40 simulation years, using the final states from the previous simulation as initial conditions for the next simulation with the same forcing until selected metrics (see Section 3.3.2) do not change within 1% tolerance. Note that the optimal number of spin-up cycles depends on the basin and the efficiency metrics used. For the sake of consistency, we looped all the simulations 10 times. The overall integrated effects emerging from using different landscape attributes are illustrated by the differences in streamflow estimates for the last (10th) repetition between two experiments with different vegetation characteristics and radiative properties, i.e., Exp1 and Exp2 in Table 4.

The long-term simulation results are analyzed first in Section 4.2.1, focusing on the overall impacts of landscape attributes data (vegetation characteristics and radiative properties together) on streamflow predictions over the four-year continuous simulations by comparing Exp1 with Exp2. Besides, the long-term impact of vegetation attributes on the regional water budget is also analyzed in Section 4.2.2 by comparing four water-year integrated water budget components between Exp1 and Exp3.

3.3.2.2. Short-term impacts. To facilitate linking cloud corrections of landscape attributes to changes in hydrological states and fluxes, we first identify a representative short-term period (e.g., a month) showing large contrast between standard MODIS data and the adjusted data we developed (i.e., effective correction to the cloud contamination) through detailed comparison in Section 4.1; then, the differences in simulated water and energy fluxes from different experiments are analyzed within the selected one month period (consistent with the analysis in Section 4.1) to evaluate day-to-day short-term impacts of the landscape attributes data. Specifically, the comparison combinations as mentioned in Section 3.3.1 including Exp1 vs. Exp3, Exp1 vs. Exp4, and Exp1 vs. Exp5 are all analyzed over this month, as discussed in Section 4.2.2 and 4.2.3.

3.3.3. Evaluation metrics

We use three dimensionless efficiency indices to evaluate hydrologic modelling performance of the simulated hydrograph, including the Nash-Sutcliffe Efficiency (NSE) (Nash and Sutcliffe, 1970), the Kling-Gupta Efficiency (KGE) (Gupta et al., 2009), and the modified KGE (KGE_{mod}) (Kling et al., 2012). The NSE (Equation (6)) measures how large the residual variance in the simulations relative to the observational variance and ranges from negative infinity to unity, with NSE = 1 indicating optimal performance. The model simulation generally is considered satisfactory if NSE > 0.50 (Moriasi et al., 2007).

$$NSE = 1 - \left(\frac{1}{n} \sum_{t=1}^n (Q_{s,t} - Q_{o,t})^2 \right) / \sigma_o^2 \quad (6)$$

where t means time step (i.e., hourly in this study), n is the total number of time steps, $Q_{*,t}$ is streamflow at time step t with * as 's' representing simulations, 'o' representing observations, and σ_o is the standard deviation of observations.

The KGE and KGE_{mod} are expressed in Eqs. (7) and (8), respectively.

$$KGE = 1 - \sqrt{(r - 1)^2 + (\beta - 1)^2 + (\alpha - 1)^2} \quad (7)$$

$$KGE_{mod} = 1 - \sqrt{(r - 1)^2 + (\beta - 1)^2 + (\gamma - 1)^2} \quad (8)$$

where r is the correlation coefficient, β is the bias ratio ($\beta = \mu_s/\mu_o$, where μ_s is the mean), α is the variability ratio ($\alpha = \sigma_s/\sigma_o$, where σ_s is the standard deviation). In KGE_{mod}, the variability ratio α was modified by Kling et al. (2012) by replacing σ_s with the coefficient of variation CV, and thus the modified variability ratio is calculated as $\gamma = CV_s/CV_o$. This simple modification ensures that the bias and variability ratios are not cross-correlated that otherwise might occur when the input precipitation is biased (Kling et al., 2012). The three components (i.e., correlation coefficient, bias ratio, and variability ratio) define a three-dimensional (3D) space. Both KGE and KGE_{mod} measure the difference between unity and the Euclidian distance in the 3D space from the ideal point (i.e., $r = 1$, $\beta = 1$, and $\alpha = 1$ or $\gamma = 1$). Thus, unity is also the optimum value for KGE and KGE_{mod}.

The three efficiency metrics described above are used to evaluate the simulated streamflow time series over the four water-years

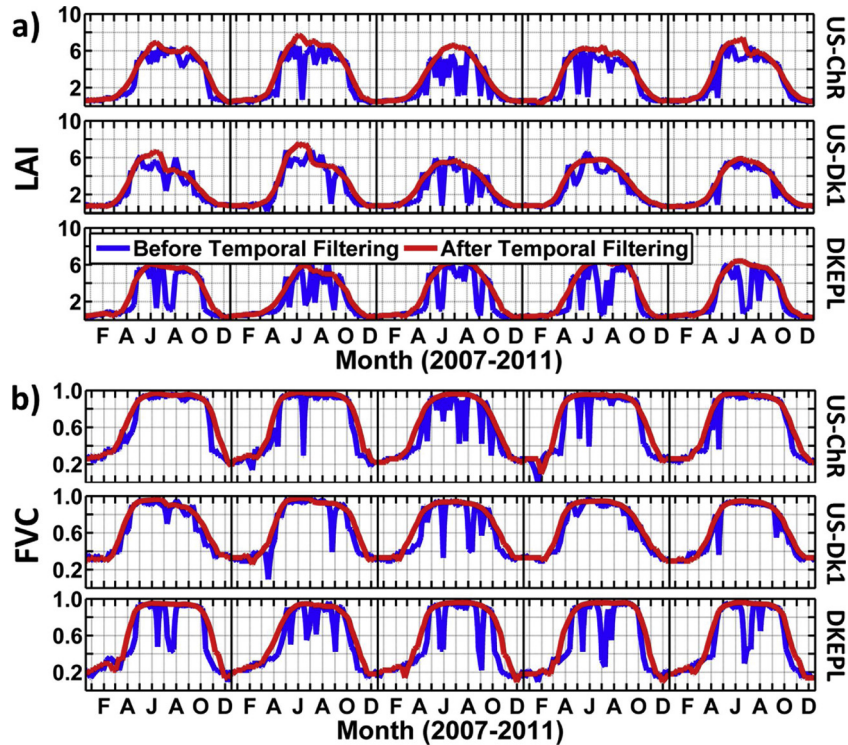


Fig. 3. Time series of LAI (a) and FVC (b) before and after temporal filtering, at two Ameriflux towers US-ChR and US-Dk1, and the DKEPL tower.

of simulation at an hourly time step. For short-term analysis of streamflow response, we mainly rely on NSE. Besides the efficiency metrics, mean square error (RMSE), mean absolute error (MAE) and mean bias error (MBE) are also used in the analysis.

4. Results

4.1. Developed LAI, FVC, emissivity, and albedo

Systematic analysis regarding the spatial pattern of the developed datasets, including mean, median, standard deviation and Probability Density Function (PDF) for each landcover type, can be found in the associated technical report (Tao and Barros, 2014b). In this section, we focus on demonstrating the removal of cloud impacts within the original MODIS vegetation and emissivity product, and how this affects the seasonal and sub-seasonal variations of LAI, FVC and emissivity, and the accuracy and rationale of the constructed albedo product.

4.1.1. LAI and FVC

Time-series of LAI and FVC before and after temporal filtering at the three tower locations are shown in Fig. 3. The land-cover classes for these towers are listed in Table 2. Although no field measurements of LAI and FVC are available for evaluation proper at these tower locations, we show the comparison of time series to illustrate how the adaptive filtering method can significantly reduce the discontinuity and errors in LAI and thus CV, improving the overall data quality. It can be seen from Fig. 3 that the adjusted LAI series preserves the inter- and intra-annual variability of the original MODIS product, and captures well the timing of the growing season, which in turn adds confidence to the FVC estimates. The LAI and FVC at the DKEPL-tower exhibit the largest change compared to other towers (largest RMSE between LAI before and after filtering, i.e., 1.40 at DKEPL versus 1.11 and 0.82 for USChR and USdk1, respectively), because the adaptive filter corrected the significant contamination of the diurnal cycle of fog and low-level clouds in the Smoky Mountains (e.g., Duan and Barros, 2017; Wilson and Barros, 2014), and at the DKEPL location in particular. For the two other towers, the most frequent contamination (dramatically reduced values) occurred during the summer time (from June to October), especially in 2009, a very wet hydrological year with frequent storm events during the Atlantic hurricane season (Brun and Barros, 2013). For example, there are virtually no cloud-free MODIS data within an 8-day period around Sep. 16 in 2009 in the IPHEX domain, a period of persistent rainfall in the SE US that resulted in severe cloud contamination of the LAI product as illustrated in the top and middle row panels in Fig. 4. The spatial distributions of the adjusted LAI and FVC 10-days before and after Sep. 16 exhibit reasonable values and distribution patterns after correction in contrast with the very low values (i.e., LAI around two shown in red color) in the standard LAI and FVC products. Two archived photographs (Fig. 4c) available in Sep. and Oct. from a webcam⁷ installed at Purchase Knob in the Pigeon River Basin show the forest status with very large LAI and FVC at the time. The contamination is

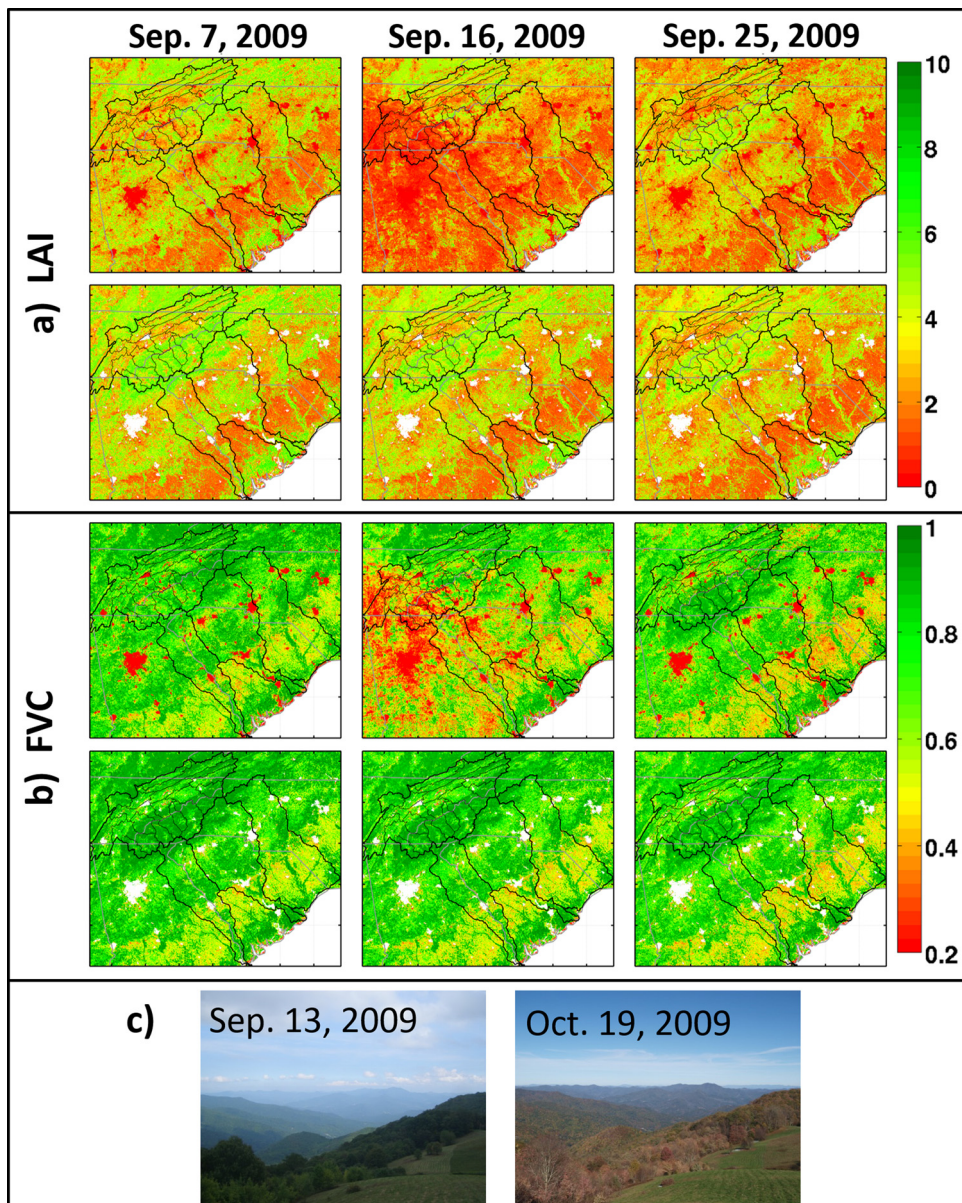


Fig. 4. Examples of the spatial distribution of LAI (a) and FVC (b) before (upper row in each panel) and after (bottom row in each panel) temporal filtering over the southeast US. Extensive cloud contamination is noticeable on Sep. 16 (center figure, top row, in each panel). Panel c) archived photos from a webcam installed in the Pigeon River Basin.

successfully removed by the TIMESAT adaptive filter, as demonstrated by the central panel in Fig. 4. These results illustrate the importance of targeted quality-control of standard products to reduce the discontinuity and abnormal values in LAI and thus FVC.

Panels a) and b) in Fig. 5 illustrate the space-time heterogeneity of LAI and FVC over the region including large seasonal and intra-seasonal variations. The northeast-to-southwest patterns of alternating high and low values are attributed to the various vegetation zones (see land-cover map Figure S1 in the supplementary file). The mixed zones of woody savanna and croplands close to the coast show low LAI all year round (top panel, Fig. 5a), in contrast to the adjacent mixed forest with persistently higher LAI; seasonality is shown more clearly in Fig. 5b. Compared to the forests in the SAM, the northeast-to-southwest mixed forest zones in between the woody savanna zones and close to the coast exhibit large FVC all year round. Note the large inter-annual variability depicted in the bottom panels in Fig. 5a–b with large differences between LAI and FVC on the same day in 2007 (a dry year) and 2009 (a wet year).

⁷http://www2.nature.nps.gov/air/webcams/parks/grsmpkcam/grsmpk_arc.cfm

⁸https://lpdaac.usgs.gov/products/modis_products_table

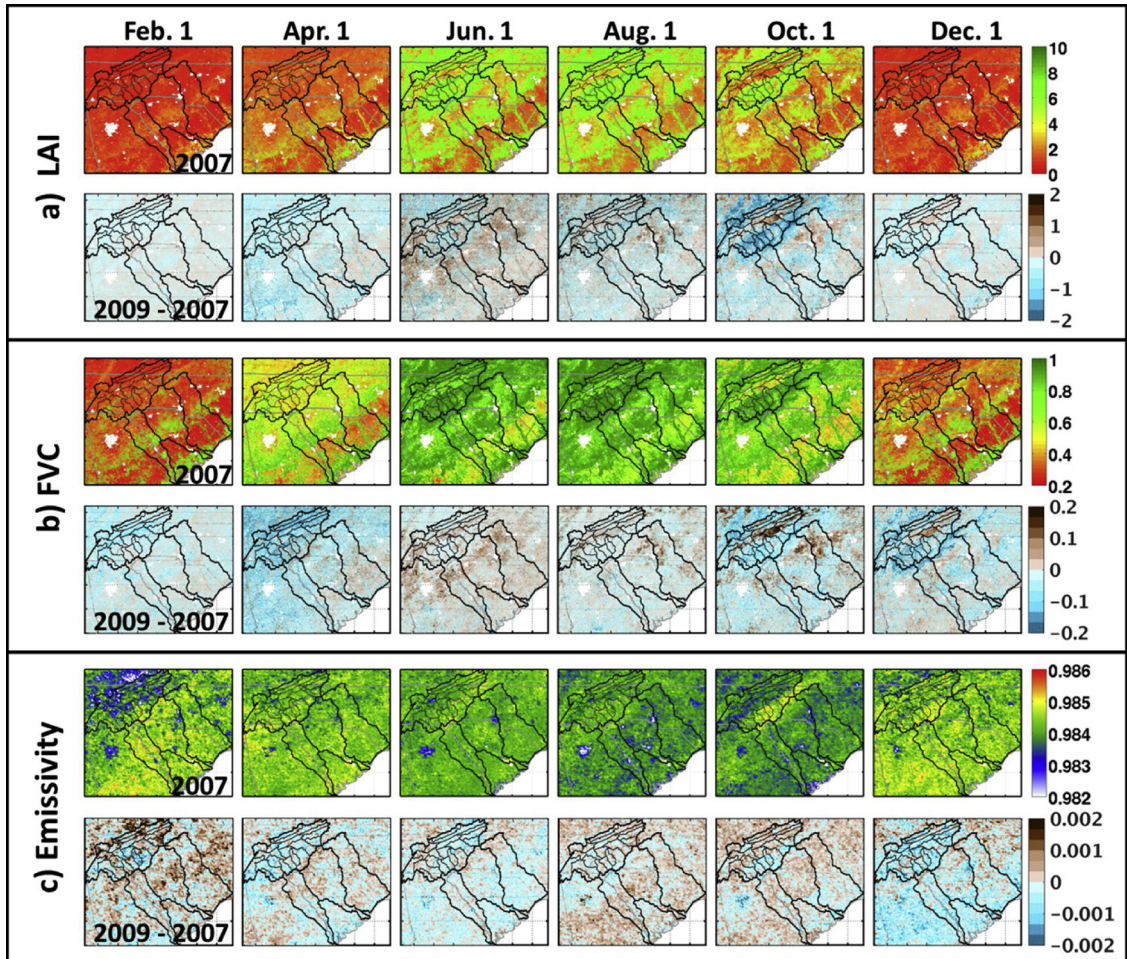


Fig. 5. Spatial distribution of LAI (a), FVC (b) and emissivity (c) on Feb.1, Apr.1, Jun.1, Aug.1, Oct.1 and Dec.1 (from left to right) in a dry year (2007, shown in the top panel for each parameter), and the difference with regard to the same day in a wet year (2009, shown in the bottom row for each parameter). The figures in the bottom panel use a symmetrical (blue-brown) color scale such that the brown color represents positive values (2007 < 2009) and the blue color represent negative values (2007 > 2009). (For interpretation of the references to color in this figure legend, the reader is referred to the web version of this article).

The frequent severe storms in August.-September of 2009 produced massive rainfall amounts over the SE US, especially over the SAM causing significant vegetation disturbance (Brun and Barros, 2013), which explains the lower LAI and FVC values on October 1 in 2009 than in 2007.

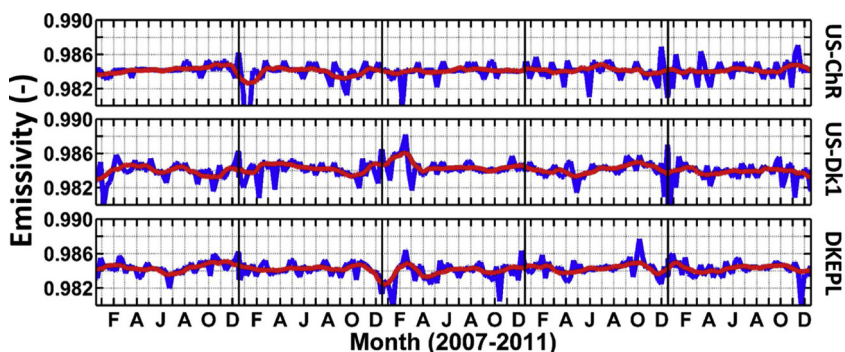


Fig. 6. Time series of the land surface broadband emissivity before and after temporal filtering at three selected Ameriflux towers.

4.1.2. Land surface longwave broadband emissivity

[Fig. 6](#) shows the land surface longwave broadband emissivity before and after temporal filtering at the selected tower locations. In contrast to LAI and FVC, for which most contamination is negatively-biased, the land surface emissivity exhibits large up-and-down fluctuations that are successfully eliminated by filtering. Generally, vegetated areas have larger emissivity than non-vegetated or sparsely vegetated areas ([Fig. 5c](#)), except for waterbodies, land-margins, and wetlands. For different types of vegetation, many factors (including vegetation species, canopy structure and density, phenology, growth stage, etc.) affect the emissivity ([Snyder et al., 1998](#)).

The top panel in [Fig. 5c](#) highlights contrasts among the Coastal Plain, the Piedmont, and the Appalachian Mountains, with large spatial heterogeneity explained by land-cover. Emissivity in urban areas (e.g., Atlanta, the largest cluster of red pixels in the IPHEx domain) remains low, although it varies temporally in response to surface wetness conditions (i.e., precipitation). Overall, for the southeast US, the top panel in [Fig. 5c](#) displays high emissivity in February over the southeast sector from the mountains to the Piedmont, and then decreases through August and October, increasing thereafter in December, a behavior that is not correlated with regional phenology. This can be explained in large part by leaf dryness (i.e., vegetation water stress) during the dry season ([Olioso et al., 2007](#)). High emissivity values in the Southern Appalachian Mountains (especially along the Blue Ridge escarpment) are associated with the seasonal leaf color change, reflecting changes in the chemical composition of the leaves. Other factors influencing emissivity include real-time vegetation growth stage, weather conditions (fog interception, rain or snow accumulation on the ground and leaves), and hydrological conditions (i.e., soil moisture conditions) ([Snyder et al., 1998](#)). The inter-annual variability in emissivity (the difference of emissivity on the same day of 2007 and 2009) illustrated in the bottom row of [Fig. 5c](#) includes both the effects of vegetation growth stage and antecedent soil moisture conditions.

4.1.3. Land surface shortwave broadband albedo

[Fig. 7a](#) compares the produced land surface shortwave broadband albedo at the Local Solar Noon (LSN) every day against the available observations at Ameriflux tower US-ChR (see [Fig. 1](#) for location). The MODIS BRDF parameters were derived for snow-free and cloud-free conditions, and thus the produced albedo are also snow-free and cloud-free. To alleviate the presence of clouds, the mean of the observed albedo within a 3-hour window centered at the LSN was calculated and then compared with the newly constructed albedo estimates, as suggested by [Román et al. \(2009\)](#). Nevertheless, it is not possible to completely filter out cloud conditions at short-times scales, even using the 3-hr mean values, which may explain the underestimation of the albedo in May. The snow conditions were identified by air temperature less than zero degrees Celsius observed at the tower (void symbols in [Fig. 7a](#)). In general, the estimated albedo shows a good agreement with observations, with a small root mean square error (RMSE = 0.017), a small mean absolute error (MAE = 0.013) and a small mean bias error (MBE = -0.007).

[Fig. 7b](#) shows the comparison of the monthly mean diurnal cycle of the newly constructed hourly albedo with the US-ChR observations. There is generally a good agreement with the tower observations except for the late afternoon, with underestimation mainly during the winter time (October to January). Further, the albedo estimates display a diurnal cycle consistent with the assumption of symmetry at LSN as indicated in the theoretical retrieval algorithm for MODIS BRDF/albedo Model ([Liu et al., 2009](#); [Schaaf et al., 2002](#)), whereas the observed albedo exhibits asymmetry. The diurnal asymmetry of observed albedo may be attributed to dew and frost formation, precipitation, evaporation and wind effects causing surfaces to look “brighter” early in the day ([Minnis et al., 1997](#)). Previous studies on the diurnal asymmetry of albedo in grassland or cropland land categories reported that albedo in the early morning is usually larger than in the afternoon ([Minnis et al., 1997](#); [Song, 1998](#)) as strong directional winds deform the vegetation canopy and turn the back of leaves upward, thus creating a brightening effect. At US-ChR, where the deciduous broadleaf forest is the dominant vegetation type ([Table 2](#)), the observed albedo has larger values in the late afternoon than in the early morning (as shown in [Fig. 7b](#)). This can be explained, at least in part, by the diurnal cycle in mountain-valley circulations as this tower is located on the foothills of the western slopes of the Appalachians in the ridge-valley region. Also, albedo also has strong seasonal variability, increasing during the growing and blooming seasons, and then decreasing during the dormant season.

The spatial distributions of BSA, WSA and the actual broadband albedo at LSN on September 2009 are presented in [Fig. 7c](#). Note the correspondence of spatial albedo patterns to those of land-cover shown in [Figure S1](#). The same albedos (BSA, WSA, and actual albedo) on June 1 and December 1 of 2009 are provided in [Figure S2](#) in the supplementary file in support of the discussion here. Wetlands along the margins of river networks exhibit very low albedo compared to other land-cover types, especially near the coast. Large spatial variability follows the complex terrain in the Southern Appalachian Mountains with contrasting values along ridges and valleys. BSA heavily depends on solar zenith angle, thus the difference between albedo at LSN in different months (June, September and December) is small due to the small differences in the solar zenith angle. WSA depends on the observed intrinsic properties of the land surface as indicated by [Equation \(4\)](#), and consequently, WSA exhibits large seasonal variations (compare middle panel in [Fig. 7c](#) and [Figure S2](#)). Inspection of the temporal evolution of the broadband albedo reveals that large seasonal albedo variations are linked directly to changes in WSA. Generally, the albedo in winter (December) is larger than in the summer (June) due to the large contrast of black/dull color in December (grey branches, dark soils, etc.) versus the bright and green colors in June, as shown in [Figure S2](#) in the supplementary file.

4.2. Hydrologic model simulations

4.2.1. Impacts of developed datasets on long-term streamflow simulation

The NSE, KGE and KGE_{mod} streamflow metrics calculated at hourly time step over the four water years (from 2007 October to 2011 September) for each spin-up cycle in the three sub-basins (WFPRB, EFPRB, and CCB) are displayed in [Fig. 8a](#) for Exp1 and Exp2. It can be seen from [Fig. 8a](#) that all skill scores from both experiments increase with repeated spin-up for the three basins, illustrating

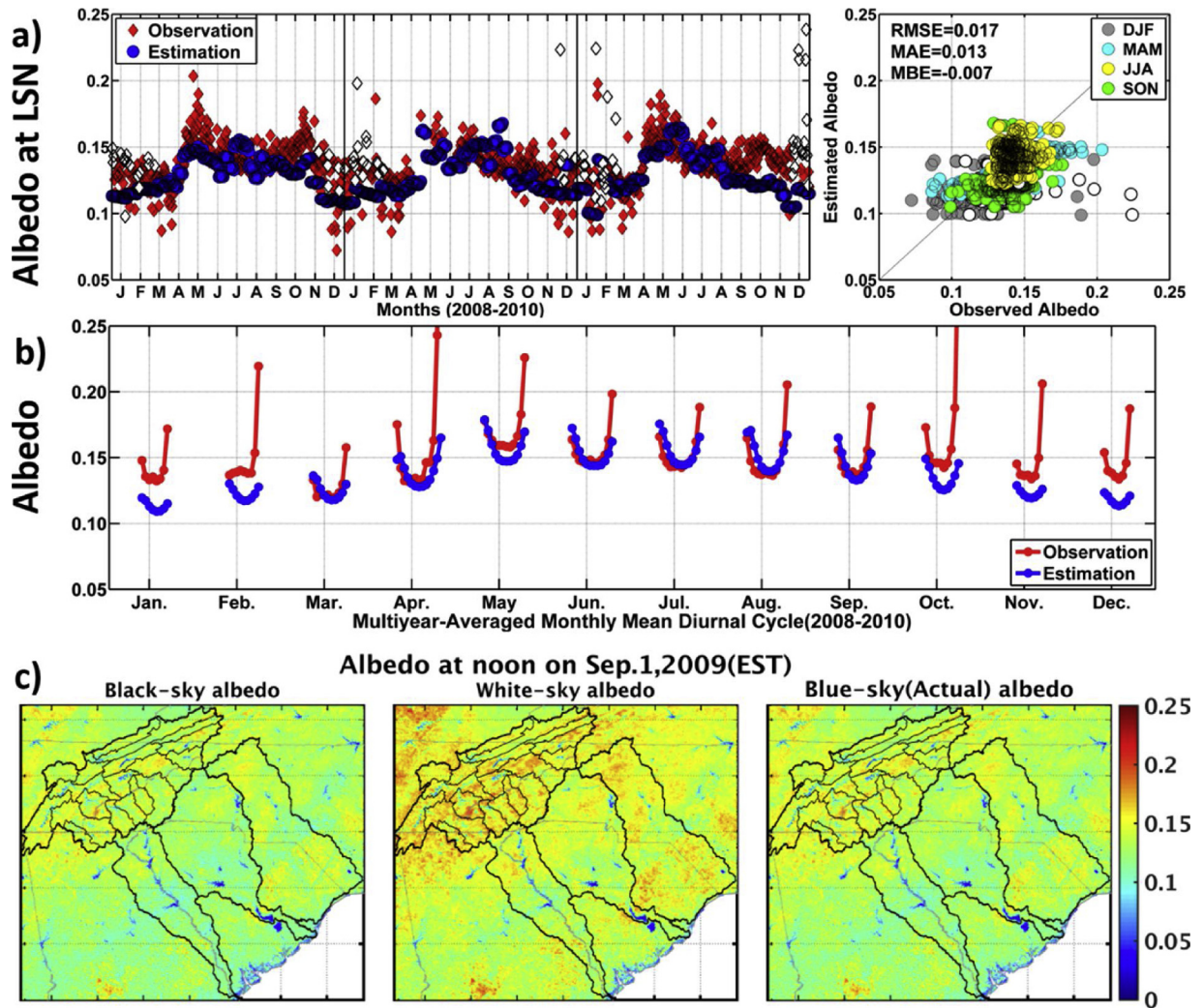


Fig. 7. a) Time series of new land surface albedo estimates at LSN constructed from MODIS BRDF parameters and observed at AmeriFlux tower US-ChR from 2008 to 2010. The symbols with void color indicate snow conditions which were identified by air temperature less than zero degrees Celsius at the tower. b) Monthly mean diurnal cycle of land surface albedo estimates and observations a 2008-2010. c) Spatial distribution of land surface albedo (BSA: Black-sky albedo; WSA: White-sky-albedo; Actual: Blue-sky albedo) at noon (EST) on September 1 in 2008 over the southeast US. (For interpretation of the references to color in this figure legend, the reader is referred to the web version of this article).

the impact of improved initial conditions on hydrologic simulation fidelity. The skill scores do reach a plateau above which further improvements are negligible after sufficient spin-up cycles, indicating that the model reached internal equilibrium and the maximum achievable predictive skill (alternatively viewed as a predictability barrier) that is different for each basin. This predictability barrier for each evaluation metric (i.e., skill scores for the last spin-up) is determined by the accuracy of input data (i.e., atmospheric forcing and landscape attributes), model parameters, and the specific basin geomorphology characteristics that affect the propagation of forcing errors through current model configuration. The predictive skill barrier could be improved through calibration (note DCHM is uncalibrated) and by improving precipitation forcing as we conducted in previous studies (Tao and Barros, 2014a, 2013; Tao et al., 2016). This is out of the scope of this study. Rather, here we analyze the differences in the evaluation metrics for the final (10th spin-up) simulation between Exp1 and Exp2 to illustrate the impacts of using different landscape attributes on streamflow simulations with known rainfall errors as discussed by Nogueira and Barros (2014, 2015) and fixed hydrologic parameters.

The three efficiency indices (NSE, KGE, and KGE_{mod}, see details in Section 3.3.2), along with the correlation coefficient (r), the bias ratio (β), the variability ratio (α) and the modified variability ratio (γ) for the last spin-up are provided in Table 6 for the three basins. The skill-score differences between Exp1 and Exp2 for WFP RB are either quite small (e.g., NSE and correlation coefficient) meaning equivalent performance, or indicate worsen performance for Exp1 than Exp2. For EFP RB, Exp1 shows slightly better NSE (0.58 vs. 0.54), equivalent KGE (0.69 vs. 0.70), but worse KGE_{mod} (0.46 vs. 0.55) than Exp2 due to the lower modified variability ratio (γ) (i.e., away from unity). This reflects the increased topographic and geomorphic complexity of this basin, as well as the fact that rainfall errors are expected to be larger due to lack of raingauge observations in the basin and ground-clutter effects on the radar

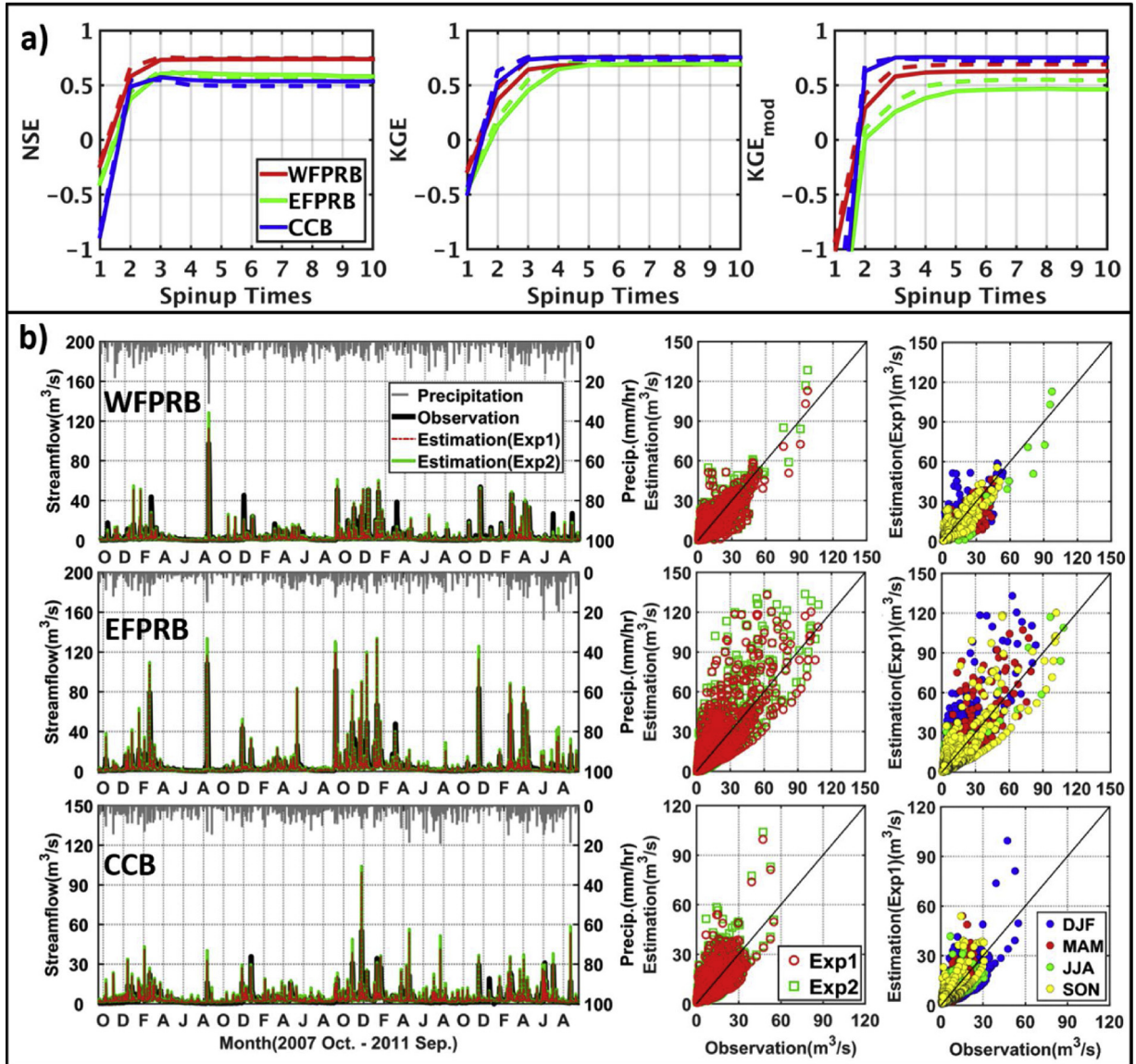


Fig. 8. Top panel (a): Evolution of the NSE, the KGE and the modified KGE (KGE_{mod}) calculated based on hourly simulation results for each spin-up cycle for the three headwater basins (solid line for Exp1 and dash line for Exp2). Bottom panel (b): left panel: time series of streamflow observations and estimations from Exp1 and Exp2 in the three headwater basins over the four water-year period (of the last spin-up); mid panel: scatter plots of streamflow observations and model estimations from Exp1(cycle) and Exp2 (square) ; right panel: scatter plots synthesize seasonal performance for Exp1.

Table 6

Metrics calculated based on four-year hourly simulation results from the 10th spinup for the three headwater basins (i.e., WFPRB, EFPRB, and CCB).

	Simulations	NSE	KGE	KGE_{mod}	r	β	α	γ
WFPRB	Exp1	0.74	0.69	0.63	0.88	0.73	0.90	1.23
	Exp2	0.75	0.76	0.69	0.88	0.80	0.96	1.20
EFPRB	Exp1	0.58	0.69	0.46	0.83	0.77	1.13	1.46
	Exp2	0.54	0.70	0.55	0.83	0.86	1.19	1.39
CCB	Exp1	0.54	0.75	0.75	0.76	1.01	0.96	0.95
	Exp2	0.49	0.73	0.72	0.76	1.12	1.03	0.92

rainfall product. The bias ratio (β) and variability ratio (both α and γ) for CCB are closest to unity (especially for Exp1), resulting in the shortest Euclidian distance between the point (r, β, α) or (r, β, γ) and the ideal point $(1, 1, 1)$ among the three basins, and thus best KGE and KGE_{mod} efficiencies (0.75 for both) are attained. Yet, the hourly NSE for CCB is comparatively low mainly due to poor performance for low flows (i.e., $< 3 \text{ m}^3/\text{s}$ as shown in Figure S3 in the supplementary file). This is attributed to Stage IV rainfall uncertainty in this inner-mountain basin below the scanning levels of regional operational radars: that is, low-level rainfall is missed whereas larger rainfall events appear to be overcorrected in the CCB (Tao and Barros, 2013; Tao et al., 2016). Nevertheless, in contrast to WFPRB, all the efficiency indices for Exp1 are better than Exp2 for the CCB (i.e., NSE, KGE, and KGE_{mod} increases by 10%, 3%, and 4%, respectively), with significantly improved performance using the newly developed landscape attributes data. As discussed in Section 2, CCB is located in the inner SAM region of the Great Smoky Mountains, and thus low level clouds, heavy fog, and light rainfall are persistent which results in severe cloud contamination to MODIS product. Consequently, the larger improvement in simulated streamflow for CCB compared to the other two basins are attributed to the effectiveness of the cloudiness correction of landscape attributes over this basin.

Fig. 8b displays the streamflow time series from the last spin-up iteration and the scatter plot of simulations against observations for the three basins. The left panel of Fig. 8b shows that Exp2 (green) overestimates streamflow for many large events using the standard MODIS vegetation products and the standard treatment for radiative properties, while Exp1 (red) shows comparatively better performance. The middle panels of Fig. 8b exhibit overall good agreement between simulated and observed streamflow for the two experiments with better performance using the corrected/adjusted vegetation and constructed radiative data sets for the larger flow events. Winter (DJF) streamflow is overestimated in all basins, likely reflecting the overestimation of radar rainfall due to bright-band artifacts (i.e., due to the presence of snow and ice lower in the atmosphere). Because of very different geomorphology and hydrometeorology, the seasonal behavior is different among the three basins as highlighted in the scatter plot in Fig. 8b. The WFPRB simulations exhibit relatively worse performance for winter storms (DJF) in contrast with very good agreement for summer flows (JJA) associated with heavy convective storm systems on the eastern slopes of the SAM. This is because summertime convective storms can be captured by the nearby National Weather Service operational radar in Greenville, South Carolina, and thus are well represented in Stage IV precipitation data. By contrast, most large flow events in the CCB occurred in the winter associated with westerly frontal storms. Further, the rainfall-runoff response is directly tied to basin geomorphologic characteristics and complex topography. WFPRB is located on the highest mountain ridges in the eastern slopes of the Appalachians, and the rainfall-runoff response is very fast due to steep slopes and shallow soils (Tao and Barros, 2013). For heavy rainfall events such as Tropical Storm Fay (the large peak in Aug. in 2008) differences in streamflow estimates are as large as $16 \text{ m}^3/\text{s}$ (~10% of peak discharge) between Exp1 and Exp2 in the WFPRB, with improved performance for Exp1 in all basins resulting in peak discharge improvements up to 20% in the EFPRB and CCB. Similar behavior is seen for the CCB throughout the year, though peak flows are lower since deep valley soils and active surface-groundwater interactions provide more storage for individual events (Tao and Barros, 2014a). In the cold season, fog and persistence of low level cloudiness in the inner region valleys (Wilson and Barros, 2014, 2017; Duan and Barros, 2017) maintain the upper soil layers wet which favors runoff response even if the rainfall intensities are lower (e.g., winter of 2009 in the EFPRB and CCB), but these are not adequately observed by the operational network used to produce the merged radar-raingauge Stage IV precipitation product.

In summary, we demonstrated a significant improvement in simulated streamflow over four water-years by using the newly developed landscape attributes data (i.e., adjusted/corrected vegetation products and constructed radiative properties) compared to the results using standard MODIS vegetation products and standard treatment to radiative properties over the CCB (e.g., the NSE calculated at an hourly time step was improved by 10%), a basin that have most severe cloud contamination to MODIS standard products among the three basins. The performance of Exp1 for EFPRB is comparable to Exp2 for EFPRB and is even worse for WFPRB, which is not unexpected under the context of current predictability barrier for each tested basin (i.e., know rainfall errors). The results substantiate the fidelity and utility of the developed landscape attributes data in simulating streamflow with distributed hydrologic models in mountainous regions.

4.2.2. Impacts of LAI and FVC on water flux simulations

The integrated impacts of landscape attributes data on streamflow estimation demonstrated in the previous section lump together the changes caused by using both adjusted vegetation characteristics and constructed radiative properties. In this section, we compare the results from Exp3 with Exp1 to illustrate the impacts of adjusted vegetation attributes (LAI and FVC) on the simulated water fluxes at both short-term and long-term scales. As indicated in Table 4, all other parameters/inputs for the DCHM are the same between the two experiments, thus any discrepancies between the two simulations are solely attributed to the difference in LAI and FVC between standard (Exp3) and adjusted (Exp1) data sets. To follow up the discussion initiated in Section 4.1.1 about the correction to the persistent cloud and precipitation contamination in MODIS vegetation product in September of 2009, here we first focus on the simulated water fluxes for the same month. Then, we analyze the cumulative difference in simulated water-budget components between the two experiments over the whole simulating period (i.e., four water-years) to illustrate the integrated impact of corrected vegetation attributes data on regional water budget (the long-term impact).

Fig. 9 shows the difference between the basin-averaged vegetation parameters and water fluxes simulated by the DCHM including rainfall interception, transpiration, evaporation, and discharge simulated for the CCB, WFPRB, and EFPRB in September of 2009. As described in the Appendix, DCHM evaporation comprises the components from the bare soil area (1-FVC) and also from the skin reservoir, including canopy retention. Since cloud contamination generally reduces the magnitude of LAI and FVC in the standard products, the LAI and FVC average adjustment mainly consisted of removing the downward peaks in the first half of September as pointed out earlier in Fig. 3 and also shown in the top two rows of Fig. 9. The corrections of LAI and FVC translate into increases in

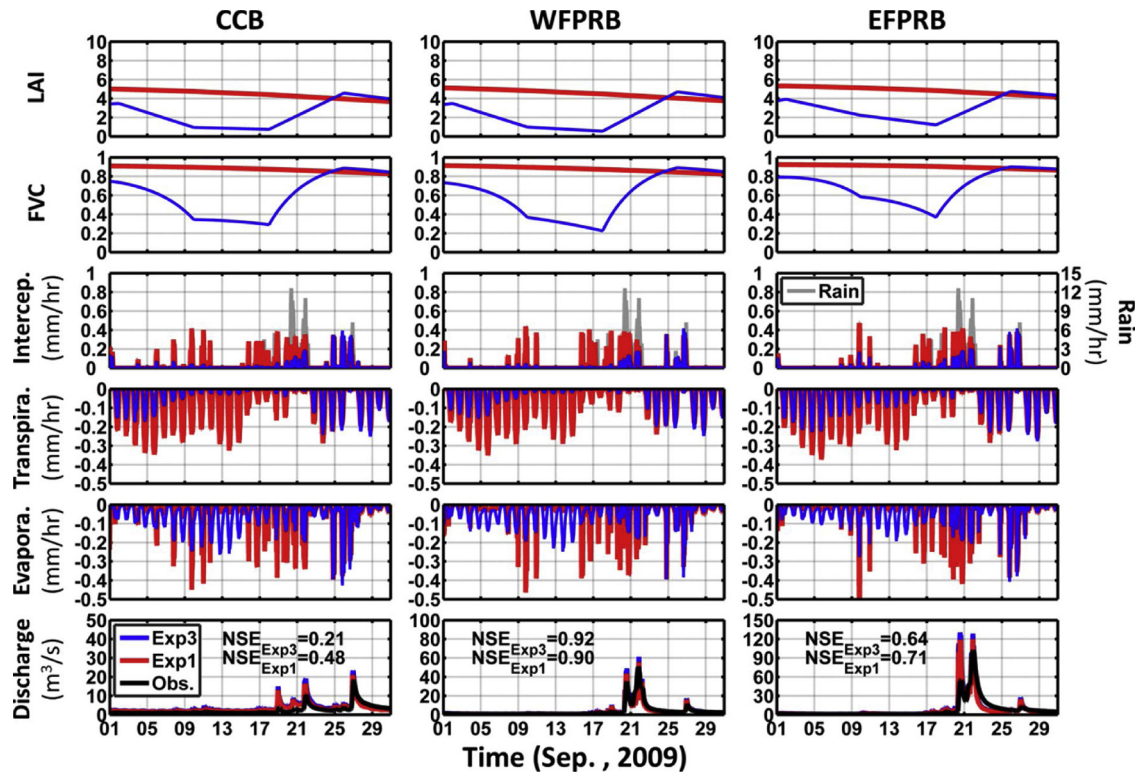


Fig. 9. Top two rows: Time series of LAI and FVC during Sep. 2009 averaged over the three headwater basins (CCB, WFPRB and EFPRB); Exp3 (blue) uses standard MODIS data, and Exp1 (red) uses the new adjusted data. The resulting intercepted rainfall (Intercep.), transpiration (Transpira.), evaporation (Evapora.) and discharge for each basin are shown from 3rd to 6th rows. The corresponding NSE scores are included in the discharge plots. (For interpretation of the references to color in this figure legend, the reader is referred to the web version of this article).

intercepted rainfall amount and transpiration in all three basins up to Sep. 25, at which time LAI and FVC before and after post-processing are very similar.

The underestimated LAI and FVC in the standard MODIS products results in lower canopy-interception capacity in the model, which is quite critical for both light rainfall and moderate-to-heavy rainstorm events. For instance, long-duration light rainfall accumulations can rapidly exceed the underestimated interception capacity with the standard MODIS products, leading to larger rainfall depths reaching the ground surface, leading to overestimation of surface runoff response and eventually streamflow. Light rainfall retained in the canopy can be used by plants via foliar uptake especially under dry conditions and, or evaporated later when a realistic canopy-interception capacity is used, that is, when vegetation is prescribed with the adjusted LAI and FVC. For moderate or heavy rainfall scenarios, more rainfall is retained in the canopy contributing to evaporation at a later time using the corrected LAI and FVC (Exp1, as illustrated by the large evaporation during heavy rainfall periods shown in the 5th row of Fig. 9), and less rainfall infiltrates into the ground, reducing soil moisture, which in turn affects transpiration and discharge. The magnitude of the corrected FVC is substantially larger than the standard product, implying therefore a similarly large change (decrease) in the bare soil areal fraction (1-FVC). Changes in FVC lead to evaporation decreases and transpiration increases (as illustrated by the large transpiration for Exp1 using adjusted vegetation attributes shown in the 4th row of Fig. 9), and lower soil moisture in the active root layers specifically. Also, considering the coupled land-atmosphere system, the differences in latent heat fluxes due to changes in evaporation and transpiration in September are significant to impact atmospheric boundary layer entropy, and ultimately enhance convective activity and rainfall in mountainous regions (e.g., Sun and Barros, 2014).

The integrated impact of using corrected vegetation parameters for the same month is examined by comparing simulated streamflow and observations in the bottom row of Fig. 9. Both streamflow simulations using the standard and adjusted vegetation attributes agree well with observed discharge with regard to peak times, although the peak values are overestimated, and more so for Exp3 than Exp1 as expected based on the above analysis. Compared to Exp3, the skill of streamflow predictions in Exp1 is substantially better by using the adjusted vegetation attributes, with NSEs at hourly time step for the month of September of 2009 increasing from 0.21 to 0.48 (i.e., more than two-fold increase) for the CCB basin in the inner mountain region largely due to improvements in the simulation of low flows. In the EFPRB, NSE changes are small (improved from 0.64 to 0.71), and they are negligible for the WFPRB (i.e., 0.92 and 0.90 for Exp3 and Exp1, respectively) demonstrating comparable or equivalent performance. This negligible difference in NSE (about 2%) for WFPRB might be attributed to interactions among different sources of error mediated by the model physics: errors in precipitation forcing compensate for using uncorrected vegetation data in Exp3, thus resulting in higher skill at the basin outlet. The large NSE gains for the CCB are attributed to the nonlinear relationship between

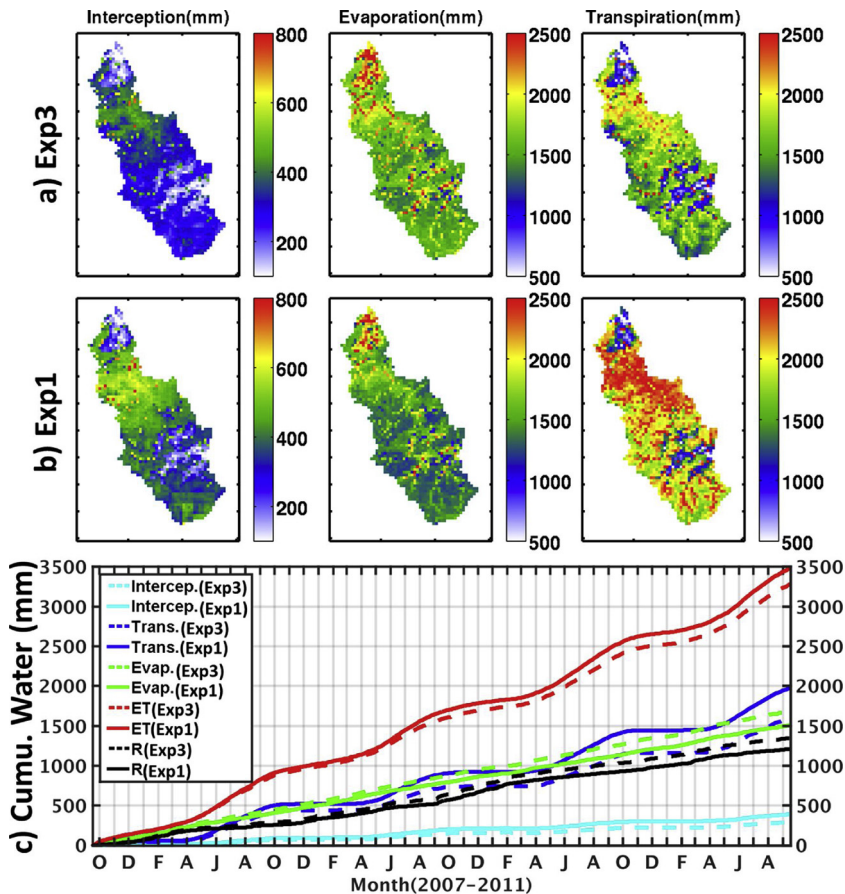


Fig. 10. Top and middle rows: spatial distribution of simulated interception, evaporation and transpiration using standard LAI and FVC (a) before (Exp3) and (b) after the adjustment (Exp1) for 2007–2011 for the Pigeon River Basin (PRB). Bottom row: (c) time series of cumulative basin-averaged Interception (Intercep.), Transpiration (Trans.), Evaporation (Evap.), Evapotranspiration (ET) and runoff(R), using standard (Exp3) and the adjusted (Exp1) LAI and FVC products over the PRB.

hydrometeorological regime (persistent low-level clouds and fog and light rainfall), geomorphology (extensive alluvial deposits and deep valley soils), and water use by vegetation (mixed forest with deciduous broad-leaf trees). The cloudiness corrections of LAI and FVC result in better estimates of interception and evapotranspiration, and consequently soil moisture; more accurate soil moisture conditions result in more accurate runoff response to rainfall and consequently improved streamflow estimation. This is also the case for the EFPRB which also features a wide alluvial valley, though the overall performance is dominated by rainfall errors in this case as shown by the large discharge error on September 20th due overestimation of rainfall for late summer convective activity.

Fig. 10 a-b shows the simulated spatial distributions of intercepted rainfall, evaporation and transpiration in the PRB using LAI and FVC before (Exp3) and after the adjustment (Exp1) accumulated over the entire four water-years to assess the impact on the regional water budget. Whereas the magnitude of the cumulative differences is small, evapotranspiration (ET) using the adjusted vegetation attributes is always larger than the ET using the standard data, and the difference is much larger in summer than in winter. The increase in ET results from large differences in transpiration in the forested areas of the CCB (Figure S1 in the supplementary file). The cumulative evaporation in Exp1 is less than that in Exp3 using standard data as shown in the 2nd column of Fig. 10a-b, indicating that the decrease in evaporation due to reduced bare soil area exceeds the increase in canopy retention over the four water-years period. Higher FVC leads to an overall increase in transpiration as shown by the 3rd column in Fig. 10a-b. Fig. 10c shows the time series of cumulative transpiration, evaporation, ET, and runoff averaged over the PRB for Exp1 and Exp3 given the same rainfall input. Again, note the nonlinear trade-offs between Exp1 and Exp3 over the 2007–2011 period among transpiration (dark blue, 25% overall increase), ET (6% increase), and runoff exiting the PRB as streamflow (10% decrease). Nevertheless, the changes in intercepted rainfall, evaporation and transpiration also depend on vegetation type. For instance, transpiration is always very small in urban areas and in mixed-use areas of cropland and woody savannahs in the northern section of the basin (as indicated in Figure S1 in the supplementary file). Large changes normally occur in mixed and deciduous forests in the inner mountain region where fog forms on a daily basis, and thus the standard MODIS vegetation attributes are more likely to suffer from cloud/fog contamination, explaining the spatial patterns on the right panels in Fig. 10a-b.

In summary, the accuracy of vegetation attributes (LAI and FVC) directly affects flood response (i.e., high-flow scenarios), water

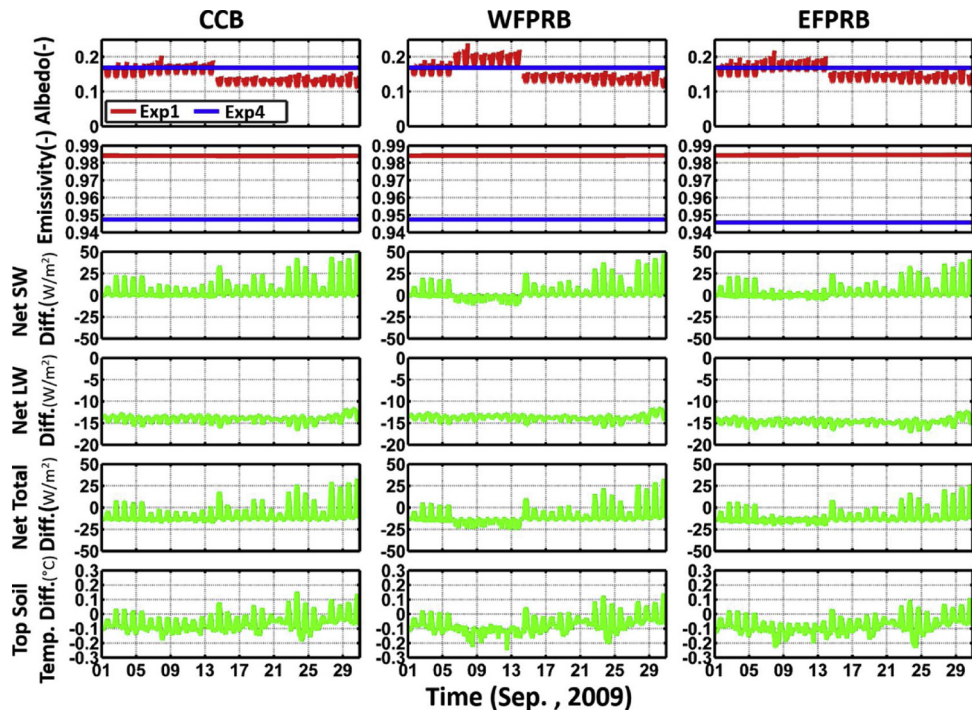


Fig. 11. Time series of albedo and emissivity during Sep. 2009 spatially averaged for each one of the three headwater basins are shown in the top two rows: Exp4 (blue) using LC-dependent emissivity and albedo, and Exp1 (red) using the new adjusted emissivity with post-processing and the new constructed spatio-temporal variant albedo from MODIS BRDF parameters. The differences between Exp1 and Exp4 (Exp1 – Exp4) for net shortwave radiation (Net SW), net longwave radiation (Net LW), the total radiation (Net Total) and the top soil temperature (Top Soil Temp) are shown in green from the third to the sixth rows, respectively. (For interpretation of the references to color in this figure legend, the reader is referred to the web version of this article).

partitioning at the basin scale, and the overall water budget in a nonlinearly complex manner. With corrected vegetation attributes, the NSE of simulated streamflow for CCB is improved by two-fold, although the improvement for EFPRB is small and the performance in WEPRB is comparable or equivalent. In addition, using corrected (and thus realistic) LAI and FVC leads to increased ET (by 6%) and decreased streamflow (by 10%) for the whole PRB over four water-years, which imposes complex constraints in water availability from the point of view of regional resilience to drought. The simulations presented here provide a first estimate of the error budget that can be attributed to vegetation characteristics in an uncalibrated model. These errors and uncertainties can be masked by model calibration, which has implications for the fidelity of the hydrological physics simulated by the model potentially leading to misinterpretation of cause-effect mechanisms as illustrated for the WFPRB. Previously, Yildiz and Barros (2007) demonstrated that LAI and FVC are as important as hydraulic conductivity to capture rainfall-runoff response in long-term hydrologic simulations using a distributed model with time-varying vegetation in the Central Appalachians. The present study explains the chain of interacting processes (rainfall, interception, evapotranspiration, soil moisture, runoff) that leads to improving streamflow prediction from improved vegetation parameters which effectively function as scaling metrics of evapotranspiration.

4.2.3. Impacts of albedo and Emissivity on energy flux simulations

In this section, the simulations from Exp4 (conventional treatment) and Exp5 (standard treatment) are compared with Exp1 (constructed realistic data) to illustrate the impacts of surface radiative properties (i.e., shortwave broadband albedo and longwave broadband emissivity) on simulations of energy fluxes. The resultant time-series of basin-averaged values over the three headwater basins are presented in Fig. 11 with a focus on the comparison between Exp1 and Exp4 (constructed vs. conventional treatment) and Figure S4 (in the supplementary file) emphasizing the difference between constructed vs. standard treatment of radiative properties (see Section 3.3.1). The amplitude range of the differences is better captured by the spatial maps in Fig. 12 a) and b) over the whole Pigeon River Basin.

The constructed hourly albedo values in the early morning or late afternoon are much larger than at LSN and exhibit large diurnal variability with a convex opening-up U shape (shown in the top row of Fig. 11, see also Fig. 7b), which is opposite of the diurnal shape for the incoming solar radiation (an opening-down U shape). Consequently, the net shortwave radiation shows larger diurnal amplitudes when using the constructed hourly albedo (Exp1) than using the LC-dependent (static) albedo (Exp4, 3rd row in Fig. 11). During September of 2009, the maximum difference in basin-averaged net shortwave radiation is up to ~ 50 W/m² for the three headwater basins. The static LC-dependent emissivity is lower (0.93 for deciduous broadleaf forest and 0.95 for the mixed forest) compared to the adjusted emissivity product (around 0.984–0.985, 2nd row in Fig. 11). The lower emissivity in Exp4 results in lower

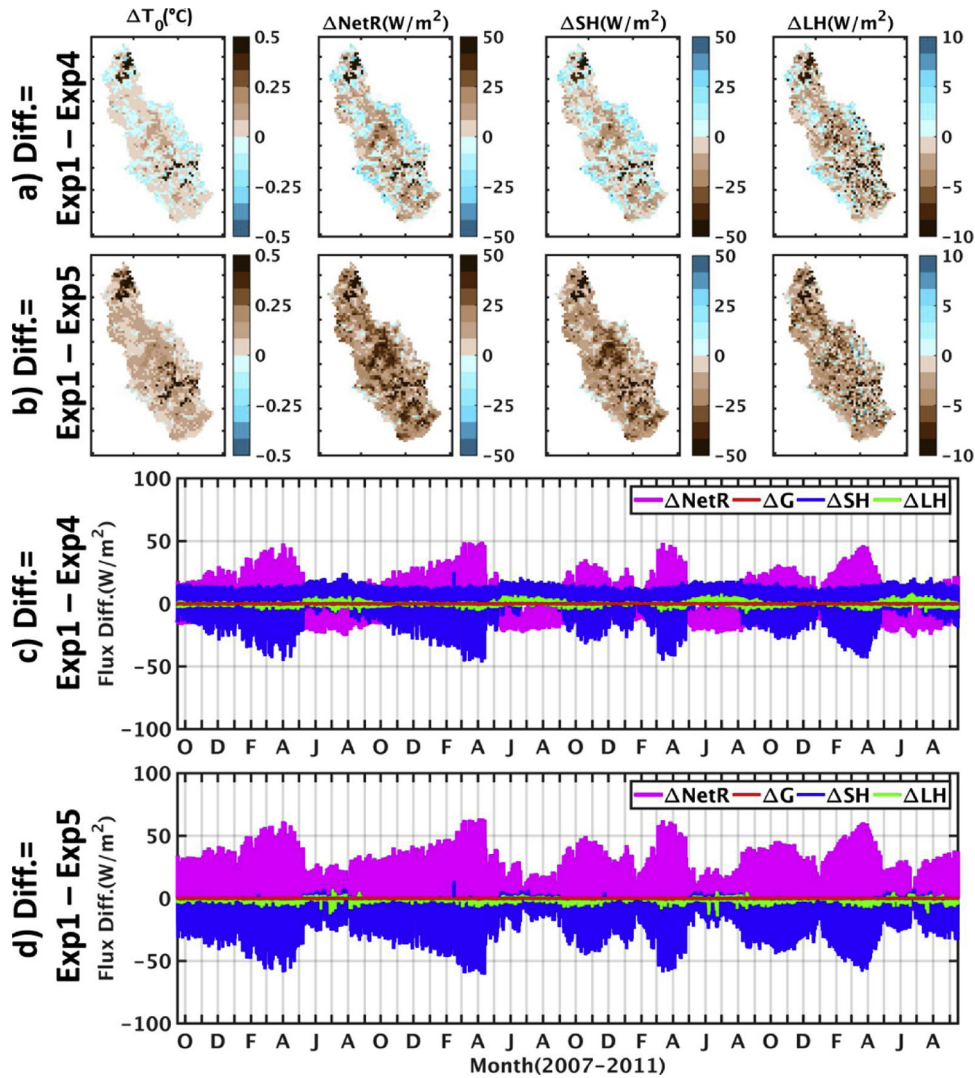


Fig. 12. Spatial distribution of differences in simulated top soil temperature, net radiation, sensible heat flux and latent heat flux from Exp1 and Exp4 runs shown in (a), and from Exp1 and Exp5 runs shown in (b), at LSN on Sep.2 of 2009 (a clear-day snapshot, more details included in a companion paper). Note the color scale is opposite for ΔSH and ΔLH to that used for $\Delta NetR$ due to opposite flux direction, i.e., upward toward atmosphere vs. downward toward ground surface. The time series of basin-averaged fluxes differences between the runs for the four water-years period over the Pigeon River Basin are shown in bottom panels (c) and (d).

outgoing longwave radiation, and thus larger net longwave radiation fluxes compared to Exp1. This explains the negative difference (-13 W/m^2 to -15 W/m^2 , 4th row in Fig. 11) between the net longwave radiation using adjusted time-varying emissivity (in Exp1) and the fixed static LC dependent emissivity (in Exp4). Overall, the negative difference in net longwave radiation explains the negative baseline (-13 W/m^2 to -15 W/m^2) in the net total radiation difference (the 5th row in Fig. 11) between Exp1 and Exp4, while the variation in net total radiation difference is still dominated by the large diurnal difference in net shortwave radiation associated with the effects of albedo. As a result, the basin-averaged top soil temperature estimates from Exp1 and Exp4 are within -0.2°C to 0.1°C in the three headwater basins, with diurnal differences following the variations in total net radiation.

Besides examining the impacts of LC-dependent emissivity, the standard emissivity data directly calculated from MODIS narrowband emissivity without correction or adjustment was utilized in Exp5 for comparison against results using the adjusted emissivity in Exp1. As shown in the top row in Figure S4, the standard emissivity varies widely due to the cloud contamination of MODIS observations, while the adjusted emissivity is slowly varying with time. The differences between the adjusted and standard MODIS emissivity are much smaller than those between time-varying and static LC-dependent emissivity. Thus, the differences in net longwave radiation between the two simulations are very small in contrast to their counterparts in Fig. 11 demonstrating that, despite uncertainty, the standard time-varying MODIS emissivity leads already to more realistic net radiation simulations than using the static LC-dependent emissivity that is conventionally used in hydrologic modeling.

The complex spatial patterns of differences in net total radiation ($\Delta NetR$) between Exp1 and Exp4 (Fig. 12a) and between Exp1

and Exp5 ([Fig. 12b](#)) are transferred to sensible heat flux (ΔSH) with spatial variability matching the land-cover patterns in the PRB basin (Figure S1 in the supplementary file). As pointed out earlier, lower values of LC-dependent emissivity result in larger net longwave radiation in Exp4 contributing to larger net total radiation than in Exp1 over the three headwater basins, thus causing negative differences depicted by the blue tones in $\Delta NetR$ in [Fig. 12a](#) (as also shown in some other areas over the PRB). The positive $\Delta NetR$ (brown tones) between Exp1 and Exp4 result from the increase of net shortwave radiation due to the lower albedo in Exp1 (as compared to the LC-dependent albedo used in Exp4, e.g., over CCB). Since differences between the adjusted (Exp1) and standard (Exp5) emissivity are very small, and thus the changes in albedo are dominant, the $\Delta NetR$ differences between Exp1 and Exp5 are positive nearly everywhere across the PRB basin ([Fig. 12b](#)). The differences in net radiation are on the order of 5–10% and translate into 10–20% differences in sensible heat flux mirroring the changes in top soil temperature (ΔT_0). The dynamic range of the differences between Exp1 and Exp4 (or Exp5) in top soil temperature over the whole PRB is 1 °C (-0.5° to 0.5° as indicated by [Fig. 12a–b](#), left most panels). Note that the top soil temperature in the DCHM is not the skin temperature proper (e.g., [Devonec and Barros, 2002](#); see also Appendix), and thus the differences are smaller than what should be expected for the land-surface skin temperature. Even if the difference in the soil temperature estimates in the top layer (5–10 cm depth) generally remains ± 0.5 °C at the pixel scale, its impacts on regional energy budget and other processes (e.g., photosynthesis) are significant especially for long-term hydro-climatic studies.

There is a strong seasonal signature in the time-series of PRB-basin averaged energy fluxes shown in [Fig. 12c](#) for the entire 4-year simulation period because of the seasonal variability of albedo ([Fig. 7a](#) and b) with larger values from May to September. Consequently, in the spring or winter seasons, especially at noon when albedo is low (as shown in [Fig. 7](#) and also top panel in [Fig. 11](#)) and the net solar radiation is large, the differences in net solar radiation between Exp1 (new hourly albedo) and Exp4 (LC-dependent albedo) are large enough to exceed the negative differences in net longwave radiation due to using LC-dependent emissivity as discussed above, leading to positive $\Delta NetR$ in [Fig. 12c](#) resulting in a sign-switch (positive to negative) from late spring to early fall (see [Fig. 11](#) for September). However, when the standard temporally-varying MODIS emissivity was used in Exp5, the $\Delta NetR$ sign-switch is not observed. [Fig. 12d](#) further shows that the positive $\Delta NetR$ (pink lines) is balanced by increases in sensible heat fluxes (thus negative ΔSH up to 50 W/m² and higher) over the four-year simulation period. In addition, the absolute magnitude of $\Delta NetR$ and ΔSH between Exp1 and Exp5 is larger than that between Exp1 and Exp4 because the (negative) net longwave radiation is much smaller in Exp5 when using the standard MODIS emissivity. Note Exp4 and Exp5 have the same vegetation attributes as Exp1, and thus differences in latent heat fluxes are very low (green lines in [Fig. 12c](#) and [12d](#)) compared to other energy balance terms.

In summary, the diurnal variation of the constructed hourly albedo leads to large diurnal amplitudes of differences in the simulated net shortwave radiation and then net total radiation. Further, the seasonal variability of the constructed albedo results in robust seasonality in the differences of simulated energy fluxes (e.g., net total radiation and sensible heat flux) over the 4-years simulated. The impact of radiative properties on total net radiation includes both the influences on net shortwave radiation and net longwave radiation, whereas the absolute magnitude of the sensitivity of total net radiation to albedo is larger than to emissivity, e.g., 50 W/m² vs. 15 W/m² in the three headwater basins. The changes, however, significantly vary case by case at pixel scale depending on the differences between the prescribed static and constructed realistic (i.e., temporally and spatially dynamic) radiative properties. These experiments illustrate the nonlinearity of the interactions among the various terms in the surface energy budget equation both in space and in time, and the importance of using time-varying radiative properties to capture seasonality.

5. Conclusions

We present an end-to-end and easy-to-follow framework to produce continuous quality-controlled and gap-free landscape attributes datasets including LAI, FVC, surface longwave broadband emissivity and shortwave broadband albedo for hydrologic modeling at a consistent spatiotemporal resolution (1 km × 1 km, hourly) from the MODIS land products over the IPHEX domain ([Barros et al., 2014](#)) in the SE US from 2007 to 2013. The LAI and FVC with adjustment (i.e. quality control and adaptive temporal filtering to correct cloud or fog contamination effects) exhibit improved space-time variability especially for mountainous regions where low-level cloud and fog are persistent. Both the broadband emissivity and albedo show realistic seasonal variability and dependence on land-cover. The newly constructed hourly broadband albedo exhibits large diurnal variability, and shows an overall good agreement with tower observations except in the late afternoon, with small underestimation during the winter time. Further, analysis of hydrologic simulations using the uncalibrated DCHM demonstrates that quality vegetation attributes (LAI and FVC) result in overall better streamflow simulations at both short and long time-scales, and that the improvements vary in time and space capturing vegetation controls at different times of the year for different hydrometeorological regimes and physiographic settings. Specifically, the NSE of simulated streamflow for a valley basin (i.e., CCB) in the inner region of the Southern Appalachian Mountains where persistent cloud and fog contamination strongly affect standard remotely-sensed vegetation data is improved by two-fold over a short-term (one-month) scale and increased by 10% over a long-term (four water-years) scale by using the adjusted data. In addition, we also found that ET increases whereas streamflow decreases due to decreases in soil moisture in the simulations with the improved vegetation attributes. Although the magnitude of the basin-integrated decrease in runoff (about 139 mm per unit area) is relatively small, considering the large drainage area of 1778 km² of the PRB, the results imply a large change in the water budget corresponding to about 247,142 m³ in four water years. This change is a significant volume of freshwater supply from a water resources management perspective: it represents roughly 21 days of freshwater demand for the population living in the basin, enough to address water needs during the most severe phase of the 2007 drought. Besides, surface radiative properties (i.e., albedo and emissivity) have strong impacts on the energy flux simulations. The absolute effects on net total radiation combine the influence on net shortwave radiation caused by using constructed temporally and spatially varying albedo and on net longwave radiation caused by using

adjusted emissivity relative to conventionally land-cover dependent or standard MODIS emissivity without adjustment. They are however dominated by the large diurnal differences in net shortwave radiation associated with the effects of albedo. For instance, the simulated basin-average net shortwave radiation using land-cover dependent albedo is much smaller (up to ~50 W/m²) than using the new dynamic albedo in the three headwater basins. Persistent differences in the net total radiation over the whole PRB translate into robust seasonal biases compared against the standard or conventional treatment for radiative properties, impacting the simulations of top soil temperature and surface energy fluxes. The results also demonstrate that using the time-varying standard MODIS emissivity without post-processing is already superior to using static land-cover based emissivity.

Nonetheless, model simulations are inevitably influenced by hydrometeorological forcing uncertainty (specifically rainfall uncertainty), and thus the results presented here are still limited by residual uncertainties, imperfect model structure, and forcing uncertainty mainly attributed to rainfall, as discussed in Section 4.2.1. This could be addressed in the future by further improving and correcting rainfall data for example using data assimilation as proposed by Tao et al. (2016).

Even in the highly idealistic scenario of perfect Quantitative Precipitation Estimates (QPEs) and Quantitative Precipitation Forecasts (QPFs), hydrological models cannot resolve the water and energy flux estimations accurately if the landscape attributes are biased or are not representative of the real conditions of the land surface due to cloud contamination or spurious calibration, which is particularly handicapping for long-term hydroclimate assessments. Thus, regionally corrected spatially and temporally varying vegetation and radiative properties reflect the dynamic nature of the Earth's surface should be routinely incorporated in modeling and forecast activities.

Data availability

All the data necessary to conduct such study are available from iphex.pratt.edu and Duke University Libraries using the Digital Object Identifiers (DOI) provided. Specifically, the downscaled (with cloudiness and topographic correction) atmospheric forcing data (DOI: 10.7924/G8RN35S6) is available at <http://dukespace.lib.duke.edu/dspace/handle/10161/8958>; the landscape attributes data (DOI: 10.7924/G8H41PBG) developed in this study is available at <http://dukespace.lib.duke.edu/dspace/handle/10161/8968>; the downscaled precipitation (DOI: 10.7924/G8MW2F2W) is at <http://dukespace.lib.duke.edu/dspace/handle/10161/8969>.

In addition, the comprehensive IPHEX hydrometeorological data are accessible at Global Hydrology Resource Center (GHRC) Distributed Active Archive Center (<https://ghrc.nsstc.nasa.gov/home/field-campaigns/iphex>) (Petersen and Barros, 2018).

Acknowledgments

This work was supported by NASA's Precipitation Measurement Missions and GPM Ground Validation Program under grants (NNX13AH39G and NNX14AE71G). We appreciate the Editor and two anonymous Reviewers for their constructive comments and suggestions.

Appendix A. Abbreviated Model Description

The Duke Coupled surface-groundwater Hydrology Model (DCHM) is a fully-distributed and physically-based land surface hydrologic model solving water and energy balance equations (AP1) and (AP9) with coupled surface-subsurface interactions. Earlier studies using evolving versions of the model formerly known as LSEBM, 1D-LSHM, and 3D-LSHM and DCHM are described in various peer-reviewed publications at spatial resolutions ranging from several kms to 100's of meters including Barros (1995); Devonec and Barros (2002); Yildiz and Barros (2005, 2007, 2009), Garcia-Quijano and Barros (2005) and Gebremichael and Barros (2006) for dynamic vegetation modelling, (Kang et al., 2013, 2012a, 2012b) coupled to a detailed snow microwave emission model, and Tao and Barros (2013, 2014a, 2018) and Tao et al. (2016). In the DCHM, each pixel represents a vertical soil column containing three or more soil layers that also serve as root layers, and a dynamic base layer overlying the regolith or the water table in the case of unconfined aquifers. Parsimonious description of key model equations can be found in (Devonec and Barros, 2002; Yildiz, 2001). The key model components relevant to this study are described below.

The energy balance equation is given by (AP1),

$$C^* h_0 \frac{\partial T_0}{\partial t} = F_R + S_h + L_h + G_h \quad (\text{AP1})$$

where the left-hand term represents the change in heat storage in the superficial soil layer, C^* is the volumetric heat capacity of the soil surface. h_0 and T_0 is the thickness and the temperature of the superficial soil layer, respectively; F_R is the total net radiation comprising net shortwave and longwave radiation, S_h is the sensible heat flux, L_h is the latent heat flux, and G_h is the ground heat flux.

Total radiative flux F_R can be expressed as,

$$F_R = F_s + F_l \quad (\text{AP2})$$

where F_s is the net solar radiation flux, $F_s = (1 - \alpha_g)F_{si}$, in which F_{si} is downward incoming solar radiation, and α_g is ground albedo; and F_l is net longwave radiation flux $F_l = F_{li} - F_{lo}$, in which F_{li} is the incoming longwave radiation and F_{lo} is the outgoing longwave radiation $F_{lo} = \sigma \varepsilon_g T_0^4$, where ε_g is the ground surface emissivity, and σ is the Stefan-Boltzmann constant (WK⁻⁴ m⁻²).

The sensible and latent heat fluxes are estimated based on the Monin-Obukhov similarity theory, which has primary assumptions

of homogeneity and quasi-stationarity of the horizontal flow field, and independence of turbulent fluxes from the height of the surface layer (Arya, 1988; Brutsaert, 1982). The theory provides dimensionless variables expressing the buoyancy effects resulting from the vertical density gradients in the stable atmosphere, neglecting molecular boundaries. The sensible heat flux S_h and latent heat flux L_h can be calculated as follows:

$$S_h = C_p \rho_a C_H |U_1| (T_1 - T_0) \quad (\text{AP3})$$

$$L_h = L_v \rho_a C_W |U_1| (q_1 - q_{\text{sat}}) \quad (\text{AP4})$$

where the subscript 1 indicates a reference level in the boundary layer at which the horizontal wind velocity U_1 , the temperature T_1 , and specific humidity q_1 are known, and should be at the same height (reference height). T_0 is the ground surface temperature. q_{sat} is the specific humidity at saturation at the ground surface. ρ_a is the density of the air. C_p is the heat capacity of the air at constant pressure. L_v is the latent heat for water vaporization. C_H and C_W are the aerodynamic drag coefficients for heat and water transfer. Eq. (AP4) applies to surfaces for which evapotranspiration takes place at its potential rate. Generally, evapotranspiration occurs at much slower rates due to resistances of soil, vegetation, and snow cover. Therefore, correction factors are applied to the equation in order to convert the potential estimates of latent heat fluxes to actual values. Given the total evapotranspiration rate, L_h can be written as:

$$L_h = L_v E_t \quad (\text{AP5})$$

where the total evapotranspiration E_t is expressed as a combination of the partial evaporation fluxes from the vegetation, skin and bare soil:

$$E_t = C_v E_{sk} + C_v E_v + (1 - C_v) E_b \quad (\text{AP6})$$

in which E_{sk} , E_v and E_b are the skin evaporation, vegetation transpiration (root uptake) and bare soil evaporation, respectively; and C_v is the fractional vegetation coverage (FVC).

Transpiration E_v is estimated based on the simplified Monteith formulation as proposed by Rountree (1991):

$$E_v = \rho_a \frac{q_1 - q_{\text{sat}}}{r_a + r_c} \quad (\text{AP7})$$

where $r_a = 1/(u_1 C_H)$ is the aerodynamic resistance, and r_c is the canopy resistance which depends on solar radiation (light control), soil moisture content, air temperature and humidity, as expressed by the Jarvis scheme following the formulation,

$$r_c = \frac{r_{c,\min}}{LAI \times f_1(F_{si})f_2(\bar{\theta})f_3(T)f_4(v_{pd})} \quad (\text{AP8})$$

where $r_{c,\min}$ is a minimal stomatal resistance value which is modulated by the influence of the limiting factors including LAI, the incoming solar radiation F_{si} , the average soil moisture in the root zone $\bar{\theta}$, the air temperature T and the water vapor deficit v_{pd} . Then f_i represents the conductance functions associated with different environmental stress factors (e.g. light, moisture and vapor pressure deficit), ranging from zero to a unity.

The water balance equation is expressed by (AP9),

$$\frac{\partial W_i}{\partial t} = G_{i-1,i} - G_{i,i+1} + D_{i+1,i} - D_{i,i-1} - q_i^{\text{sub}} + q_i^{\text{in}} - q_i^{\text{out}} \quad (\text{AP9})$$

where W_i indicates soil water depth in the i^{th} soil layer, and i is from 1 to $N-1$ with N as the total number of soil layers. The $G_{i,i+1}$ represents the vertically downward gravitational drainage flux from the i^{th} to the $(i+1)^{\text{th}}$ soil layer calculated following Campbell (1974). The $D_{i+1,i}$ is the upward diffusive flux from the $(i+1)^{\text{th}}$ to the i^{th} layer and is based on moisture gradient between the two layers. The diffusion coefficient D_c is assumed to be $K/1000$. The q_i^{sub} is the subsurface flow produced in the i^{th} soil layer. For instance, q_i^{sub} is the interflow when the i^{th} soil layer is in the unsaturated zone, and q_i^{sub} is the baseflow if the soil layer is under the water table, i.e., in the saturated zone. The q_i^{in} and q_i^{out} are the extra input and output flow for the i^{th} soil layer. When $i=1$, $q_i^{\text{in}} = f$ where f is the infiltration rate and q_i^{out} is the sum of bare soil evaporation E_b , root uptake (transpiration E_v) and, if it occurs, the saturation excess overland flow. While $i>1$, q_i^{in} vanishes, and q_i^{out} is equal to the root uptake (transpiration) in the i^{th} layer.

Infiltration is described by the Green-Ampt model (Green and Ampt, 1911), (AP10) $f = K(\theta)[1 + \frac{(\phi - \theta_i)S_f}{F}]$ where f is infiltration rate [L/T]. $K(\theta) = K_s(\frac{\theta}{\phi})^n$ is vertical hydraulic conductivity [L/T], where K_s is the saturated hydraulic conductivity, θ is the soil water content, ϕ is the porosity, and n is a soil parameter, $n = 3 + 2/\lambda$ in which λ is the pore-size index (Campbell, 1974; Clapp and Hornberger, 1978; Rawls et al., 1993). S_f is the effective suction head at the wetting front [L], which moves water downward into the unsaturated zone; ϕ is effective soil porosity [L^3/L^3]; θ_i is the initial soil moisture content [L^3/L^3]. F is accumulated infiltration [L]. The wetting front suction head, hydraulic conductivity and porosity are assigned according to standard USDA soil textures classes. A 2D finite-element solution of Richard's equation to describe infiltration was implemented after Yeh and Cheng (1994) but due to high computational requirements has not been used in practice.

Rainfall interception and then retention on the canopy (P_c) is obtained by solving the water balance equation of canopy layer (stemflow is ignored),

$$\frac{\partial W_s}{\partial t} = W_s^c - E_{sk} \quad (\text{AP11})$$

where W_s is the canopy skin reservoir storage. The interception capacity $W_s^c = \min[W_s^p, W_s^a]$, in which W_s^p is the potential water that can be intercepted $W_s^p = LAI \times eR$ (the scaling factor e is assumed as 0.1), W_s^a is the available skin reservoir storage ($W_s^a = W_s^{max} - W_s(t-1)$), with W_s^{max} as the maximum skin reservoir storage (storage capacity) ($W_s^{max} = F \times LAI$, $F = 0.1$ mm following (Dickinson et al., 1993, 1991)), and $W_s(t-1)$ as the skin reservoir storage at the previous step. Then $P_c = \min[C_v W_s^c, P]$, where P is the rainfall input. Temporal delays in throughfall are neglected. The effective rainfall reaching ground surface then is $P_{eff} = P - P_c$.

The excess water that does not infiltrate and remains at the ground surface becomes (infiltration excess) overland flow (combined with saturation excess overland flow) and then is routed by the surface flow routing model based on the kinematic wave approximation assuming a linear flow surface across grid cells (Yildiz and Barros, 2007). A diffusion wave approximation of the Saint-Venant equations for overland flow was also implemented in the model, although was not used here for such small basins in mountainous region. After the vertical water flux (infiltration and gravity flux) are resolved, subsurface flow (interflow and baseflow components) is estimated at each grid element in each soil layer, and then is routed to channel segments using a modified multi-cell approach (Bear, 1979). Channel flow routing uses the Muskingum-Cunge method of variable parameters (Ponce and Yevjevich, 1978) neglecting backwater effects.

Appendix B. Supplementary data

Supplementary material related to this article can be found, in the online version, at doi:<https://doi.org/10.1016/j.ejrh.2019.100596>.

References

- Andersen, J., Dybkjaer, G., Jensen, K.H., Refsgaard, J.C., Rasmussen, K., 2002. Use of remotely sensed precipitation and leaf area index in a distributed hydrological model. *J. Hydrol. (Amst)* 264 (1-4), 34–50.
- Arya, S.P., 1988. Introduction to Micrometeorology. Academic Press, Inc, San Diego, CA.
- Baldwin, M.E., Mitchell, K.E., 1998. Progress on the NCEP Hourly Multi-sensor US Precipitation Analysis for Operations and GCIP Research. *World Meteorological Organization-Publications-WMO TD: 1 7-1.8.*
- Baret, F., et al., 2013. GEOV1: LAI and FAPAR essential climate variables and FCOVER global time series capitalizing over existing products. Part1: principles of development and production. *Remote Sens. Environ.* 137, 299–309.
- Barros, A.P., 1995. Adaptive multilevel modeling of land-atmosphere interactions. *J. Clim.* 8 (9), 2144–2160.
- Barros, A.P., et al., 2014. NASA GPM-Ground Validation: Integrated Precipitation And Hydrology Experiment 2014 Science Plan. Duke University, Durham, NC. <https://doi.org/10.7924/G8CC0XMR>.
- Bear, J., 1979. Hydraulics of Groundwater. McGraw-Hill Book Co, New York.
- Bonan, G.B., 1996. Land Surface Model (LSM Version 1.0) for Ecological, Hydrological, and Atmospheric Studies: Technical Description and Users Guide. Technical note. National Center for Atmospheric Research, Boulder, CO United States.
- Brun, J., Barros, A.P., 2013. Vegetation activity monitoring as an indicator of eco-hydrological impacts of extreme events in the southeastern USA. *Int. J. Remote Sens.* 34 (2).
- Brutsaert, W., 1982. Evaporation Into the Atmosphere: Theory, History, and Applications. Reidel; Sold and distributed in the U.S.A. and Canada by Kluwer Boston, Dordrecht, Holland; Boston; Hingham, MA.
- Camacho, F., Cemicharo, J., Lacaze, R., Baret, F., Weiss, M., 2013. GEOV1: LAI, FAPAR essential climate variables and FCOVER global time series capitalizing over existing products. Part 2: Validation and intercomparison with reference products. *Remote Sens. Environ.* 137, 310–329.
- Campbell, G.S., 1974. A simple method for determining unsaturated conductivity from moisture retention data. *Soil Sci.* 117 (6), 311–314.
- Cedilnik, J., Carrer, D., Mahfouf, J.F., Roujeau, J.L., 2012. Impact assessment of daily satellite-derived surface albedo in a limited-area NWP model. *J. Appl. Meteorol. Climatol.* 51 (10), 1835–1854.
- Cescatti, A., et al., 2012. Intercomparison of MODIS albedo retrievals and in situ measurements across the global FLUXNET network. *Remote Sens. Environ.* 121, 323–334.
- Chen, F., Janjić, Z., Mitchell, K., 1997. Impact of atmospheric surface-layer parameterizations in the new land-surface scheme of the NCEP mesoscale Eta model. *Boundary Meteorol.* 85 (3), 391–421.
- Chen, J.M., Chen, X.Y., Ju, W.M., Geng, X.Y., 2005. Distributed hydrological model for mapping evapotranspiration using remote sensing inputs. *J. Hydrol. (Amst)* 305 (1-4), 15–39.
- Choudhury, B.J., 1987. Relationships between vegetation indices, radiation absorption, and net photosynthesis evaluated by a sensitivity analysis. *Remote Sens. Environ.* 22 (2), 209–233.
- Choudhury, B.J., Ahmed, N.U., Ido, S.B., Reginato, R.J., Daughtry, C.S.T., 1994. Relations between evaporation coefficients and vegetation indexes studied by model simulations. *Remote Sens. Environ.* 50 (1), 1–17.
- Clapp, R.B., Hornberger, G.M., 1978. Empirical equations for some soil hydraulic properties. *Water Resour. Res.* 14 (4), 601–604.
- Csiszar, I., Gutman, G., 1999. Mapping global land surface albedo from NOAA AVHRR. *J. Geophys. Res. Atmos.* 104 (D6), 6215–6228.
- Das, P., et al., 2018. Impact of LULC change on the runoff, base flow and evapotranspiration dynamics in eastern Indian river basins during 1985–2005 using variable infiltration capacity approach. *J. Earth Syst. Sci.* 127 (2).
- Dash, P., Gottsch, F.M., Olesen, F.S., Fischer, H., 2002. Land surface temperature and emissivity estimation from passive sensor data: theory and practice-current trends. *Int. J. Remote Sens.* 23 (13), 2563–2594.
- Devonec, E., Barros, A.P., 2002. Exploring the transferability of a land-surface hydrology model. *J. Hydrol. (Amst)* 265 (1-4), 258–282.
- Dickinson, R.E., Kennedy, P., 1992. Impacts on regional climate of amazon deforestation. *Geophys. Res. Lett.* 19 (19), 1947–1950.
- Dickinson, R.E., Henderson-Sellers, A., Rosenzweig, C., Sellers, P.J., 1991. Evapotranspiration models with canopy resistance for use in climate models, a review. *Agric. For. Meteorol.* 54, 2–4.
- Dickinson, R.E., Henderson-Sellers, A., Kennedy, P.J., 1993. Biosphere-Atmosphere Transfer Scheme (BATS) version 1e as coupled to the NCAR community climate model. NCAR Technical Note: NCAR/TN-387+STR.
- Dirmeyer, P.A., Shukla, J., 1994. Albedo as a modulator of climate response to tropical deforestation. *J. Geophys. Res. Atmos.* 99 (D10), 20863–20877.
- Duan, Y., Barros, A.P., 2017. Understanding how low-level clouds and fog modify the diurnal cycle of orographic precipitation using in situ and satellite observations. *Remote Sens. Basel* 9 (9), 920.
- Ducharne, A., Koster, R.D., Suarez, M.J., Stieglitz, M., Kumar, P., 2000. A catchment-based approach to modeling land surface processes in a general circulation model 2. Parameter estimation and model demonstration. *J. Geophys. Res. Atmosp.* 105 (D20), 24823–24838.

- Ek, M.B., et al., 2003. Implementation of Noah land surface model advances in the National Centers for Environmental Prediction operational mesoscale Eta model. *J. Geophys. Res. Atmosph.* 108 (D22).
- Eklundh, L., Jönsson, P., 2012. Timesat 3.1 Software Manual.
- Eklundh, L., Johansson, T., Solberg, S., 2009. Mapping insect defoliation in Scots pine with MODIS time-series data. *Remote Sens. Environ.* 113 (7), 1566–1573.
- Farr, T.G., et al., 2007. The shuttle radar topography mission. *Rev. Geophys.* 45 (2).
- Ford, T.W., Quiring, S.M., 2013. Influence of MODIS-derived dynamic vegetation on VIC-simulated soil moisture in Oklahoma. *J. Hydrometeorol.* 14 (6), 1910–1921.
- Forster, P., et al., 2007. Changes in atmospheric constituents and in radiative forcing. Chapter 2. Climate Change 2007. The Physical Science Basis.
- French, A.N., Schmugge, T.J., Kustas, W.P., Brubaker, K.L., Prueger, J., 2003a. Surface energy fluxes over El Reno, Oklahoma, using high-resolution remotely sensed data. *Water Resour. Res.* 39 (6).
- French, A.N., Schmugge, T.J., Kustas, W.P., Brubaker, K.L., Prueger, J., 2003b. Surface energy fluxes over El Reno, Oklahoma, using high-resolution remotely sensed data. *Water Resour. Res.* 39 (6), 1164.
- Galdos, F.V., Alvarez, C., García, A., Revilla, J.A., 2012. Estimated distributed rainfall interception using a simple conceptual model and Moderate Resolution Imaging Spectroradiometer (MODIS). *J. Hydrol. (Amst)* 468, 213–228.
- Gao, F., et al., 2008. An algorithm to produce temporally and spatially continuous MODIS-LAI time series. *IEEE Geosci. Remote Sci.* 5 (1), 60–64.
- Garcia-Quijano, J.F., Barros, A.P., 2005. Incorporating canopy physiology into a hydrological model: photosynthesis, dynamic respiration, and stomatal sensitivity. *Ecol. Model.* 185 (1), 29–49.
- Garratt, J.R., 1993. Sensitivity of climate simulations to land-surface and atmospheric boundary-layer treatments - a review. *J. Clim.* 6 (3), 419–449.
- Gebremichael, M., Barros, A.P., 2006. Evaluation of MODIS gross primary productivity (GPP) in tropical monsoon regions. *Remote Sens. Environ.* 100 (2), 150–166.
- Green, W.H., Ampt, G.A., 1911. Studies on soil physics Part I - the flow of air and water through soils. *J. Agric. Sci.* 4, 1–24.
- Gupta, H.V., Kling, H., Yilmaz, K.K., Martinez, G.F., 2009. Decomposition of the mean squared error and NSE performance criteria: implications for improving hydrological modelling. *J. Hydrol. (Amst)* 377 (1-2), 80–91.
- Heumann, B.W., Sequist, J.W., Eklundh, L., Jonsson, P., 2007. AVHRR derived phenological change in the Sahel and Soudan, Africa, 1982–2005. *Remote Sens. Environ.* 108 (4), 385–392.
- Jin, M.L., Liang, S.L., 2006. An improved land surface emissivity parameter for land surface models using global remote sensing observations. *J. Clim.* 19 (12), 2867–2881.
- Jin, Y.F., et al., 2012. The influence of burn severity on postfire vegetation recovery and albedo change during early succession in North American boreal forests. *J. Geophys. Res.-Biogeog.* 117.
- Kang, D.H., Barros, A.P., 2012a. Observing system simulation of snow microwave emissions over data sparse regions-part I: single layer physics. *IEEE Trans. Geosci. Remote. Sens.* 50 (5), 1785–1805.
- Kang, D.H., Barros, A.P., 2012b. Observing system simulation of snow microwave emissions over data sparse regions-part II: multilayer physics. *IEEE Trans. Geosci. Remote. Sens.* 50 (5), 1806–1820.
- Kang, D., Barros, A., Déry, S., 2013. Evaluating Passive Microwave Radiometry for the Dynamical Transition From Dry to Wet Snowpacks. *IEEE Transactions on Geoscience and Remote Sensing.*
- Kaufmann, R.K., et al., 2000. Effect of orbital drift and sensor changes on the time series of AVHRR vegetation index data. *IEEE Trans. Geosci. Remote. Sens.* 38 (6), 2584–2597.
- Kling, H., Fuchs, M., Paulin, M., 2012. Runoff conditions in the upper Danube basin under an ensemble of climate change scenarios. *J. Hydrol. (Amst)* 424, 264–277.
- Koster, R.D., Suarez, M.J., 1992. Modeling the land surface boundary in climate models as a composite of independent vegetation stands. *J. Geophys. Res. Atmos.* 97 (D3), 2697–2715.
- Koster, R.D., Suarez, M.J., Ducharme, A., Stiegler, M., Kumar, P., 2000. A catchment-based approach to modeling land surface processes in a general circulation model 1. Model structure. *J. Geophys. Res. Atmos.* 105 (D20), 24809–24822.
- Kumar, S.V., et al., 2006. Land information system: an interoperable framework for high resolution land surface modeling. *Environ. Model. Softw.* 21 (10), 1402–1415.
- Kumar, A., et al., 2011. Evaluation of a photosynthesis-based canopy resistance formulation in the noah land-surface model. *Boundary. Meteorol.* 138 (2), 263–284.
- Kumar, A., Chen, F., Barlage, M., Ek, M.B., Niyogi, D., 2014. Assessing impacts of integrating MODIS vegetation data in the weather research and forecasting (WRF) model coupled to two different canopy-resistance approaches. *J. Appl. Meteorol. Climatol.* 53 (6), 1362–1380.
- Lawrence, D.M., Slingo, J.M., 2004. An annual cycle of vegetation in a GCM. Part II: global impacts on climate and hydrology. *Clim. Dynam.* 22 (2-3), 107–122.
- Liang, X., Lettemaier, D.P., Wood, E.F., Burges, S.J., 1994. A simple hydrologically based model of land surface water and energy fluxes for general circulation models. *J. Geophys. Res. Atmos.* 99 (D7), 14415–14428.
- Liang, S., Strahler, A.H., Walthall, C., 1999. Retrieval of land surface albedo from satellite observations: a simulation study. *J. Appl. Meteorol. Climatol.* 38 (6), 712–725.
- Liang, S., et al., 2014. Global LAAnd Surface Satellite (GLASS) Products Algorithms, Validation and Analysis. Springer, Cham Heidelberg New York Dordrecht London.
- Lin, Y., Mitchell, K., 2005. The NCEP stage II/IV hourly precipitation analyses: development and applications. 19th Conf. on Hydrology, Amer. Meteor. Soc.
- Liu, Y.Q., 2011. A numerical study on hydrological impacts of forest restoration in the southern United States. *Ecohydrology* 4 (2), 299–314.
- Liu, J.C., et al., 2009. Validation of Moderate Resolution Imaging Spectroradiometer (MODIS) albedo retrieval algorithm: dependence of albedo on solar zenith angle. *J. Geophys. Res. Atmos.* 114.
- Liu, N.F., et al., 2013. A statistics-based temporal filter algorithm to map spatiotemporally continuous shortwave albedo from MODIS data. *Hydrol. Earth Syst. Sci. Discuss.* 17 (6), 2121–2129.
- Long, D., Singh, V.P., Li, Z.L., 2011. How sensitive is SEBAL to changes in input variables, domain size and satellite sensor? *J. Geophys. Res. Atmos.* 116.
- Lopez-Burgos, V., Gupta, H.V., Clark, M., 2013. Reducing cloud obscuration of MODIS snow cover area products by combining spatio-temporal techniques with a probability of snow approach. *Hydrol. Earth Syst. Sci. Discuss.* 17 (5), 1809–1823.
- Lowman, L.E., Barros, A.P., 2018. Predicting canopy biophysical properties and sensitivity of plant carbon uptake to water limitations with a coupled eco-hydrological framework. *Ecol. Model.* 372, 33–52.
- Mahanama, S.P., et al., 2015. Land Boundary Conditions for the Goddard Earth Observing System Model Version 5 (GEOS-5) Climate Modeling System: Recent Updates and Data File Descriptions.
- Mahfouf, J.F., Manzi, A.O., Noilhan, J., Giordani, H., Deque, M., 1995. The land-surface scheme ISBA within the Meteo-France climate model ARPEGE. Part 1: Implementation and preliminary results. *J. Clim.* 8 (8).
- Mahrt, L., Ek, M., 1984. The influence of atmospheric stability on potential evaporation. *J. Clim. Appl. Meteorol.* 23 (2), 222–234.
- Mahrt, L., Pan, H., 1984. A two-layer model of soil hydrology. *Boundary. Meteorol.* 29 (1), 1–20.
- Marin, C.T., Bouten, W., Sevink, J., 2000. Gross rainfall and its partitioning into throughfall, stemflow and evaporation of intercepted water in four forest ecosystems in western Amazonia. *J. Hydrol. (Amst)* 237 (1-2), 40–57.
- Masson, V., Champeaux, J.L., Chauvin, F., Meriguet, C., Lacaze, R., 2003. A global database of land surface parameters at 1-km resolution in meteorological and climate models. *J. Clim.* 16 (9), 1261–1282.
- Miller, D.A., White, R.A., 1998. A Conterminous United States Multi-layer Soil Characteristics Data Set for Regional Climate and Hydrology Modeling, Earth Interactions, 2. Web-based publication, Res. Citeseer.
- Minnis, P., Mayor, S., Smith, W.L., Young, D.F., 1997. Asymmetry in the diurnal variation of surface albedo. *IEEE Trans. Geosci. Remote. Sens.* 35 (4), 879–891.
- Mitchell, K.E., et al., 2004. The multi-institution North American Land Data Assimilation System (NLDAS): utilizing multiple GCIP products and partners in a continental distributed hydrological modeling system. *J. Geophys. Res. Atmos.* (D7), 109.
- Moriasi, D.N., et al., 2007. Model evaluation guidelines for systematic quantification of accuracy in watershed simulations. *Trans. ASABE* 50 (3), 885–900.
- Myneni, R.B., et al., 2002. Global products of vegetation leaf area and fraction absorbed PAR from year one of MODIS data. *Remote Sens. Environ.* 83 (1-2), 214–231.
- Nash, J.E., Sutcliffe, J.V., 1970. River flow forecasting through conceptual models part I — a discussion of principles. *J. Hydrol. (Amst)* 10 (3), 282–290.

- Niu, G.Y., et al., 2011. The community Noah land surface model with multiparameterization options (Noah-MP): 1. Model description and evaluation with local-scale measurements. *J. Geophys. Res. Atmos.* 116.
- Nogueira, M., Barros, A., 2014. The Integrated Precipitation and Hydrology Experiment - Hydrologic Applications for the Southeast US (IPHEX-H4SE) Part III: High-resolution Ensemble Rainfall Products. Report EPL-2013-IPHEX-H4SE-3, EPL/Duke University (Pub.) 80.
- Nogueira, M., Barros, A., 2015. Transient stochastic downscaling of quantitative precipitation estimates for hydrological applications. *J. Hydrol. (Amst)* 529, 1407–1421.
- Oleson, K.W., et al., 2003. Assessment of global climate model land surface albedo using MODIS data. *Geophys. Res. Lett.* (8), 30.
- Olioso, A., Soria, G., Sobrino, J., Duchemin, B., 2007. Evidence of low land surface thermal infrared emissivity in the presence of dry vegetation. *IEEE Geosci Remote Sci.* 4 (1), 112–116.
- Pan, H.-L., Mahrt, L., 1987. Interaction between soil hydrology and boundary-layer development. *Boundary. Meteorol.* 38 (1-2), 185–202.
- Park, A., Cameron, J.L., 2008. The influence of canopy traits on throughfall and stemflow in five tropical trees growing in a Panamanian plantation. *For. Ecol. Manage.* 255 (5-6), 1915–1925.
- Parr, D., Wang, G.L., Bjerkle, D., 2015. Integrating remote sensing data on evapotranspiration and leaf area index with hydrological modeling: impacts on model performance and future predictions. *J. Hydrometeorol.* 16 (5), 2086–2100.
- Petersen, W., Barros, A.P., 2018. GPM Ground Validation Integrated Precipitation and Hydrology Experiment (IPHEX) Field Campaign Data Collection. NASA EOSDIS Global Hydrology Resource Center Distributed Active Archive Center, Huntsville, Alabama, USA. <https://doi.org/10.5067/GPMGV/IPHEX/DATA101>.
- Ponce, V.M., Yevjevich, V., 1978. Muskingum-cunge method with variable parameters. *J. Hydraulics Division-Asce* 104 (12), 1663–1667.
- Pryor, S.C., Sullivan, R.C., Wright, T., 2016. Quantifying the roles of changing albedo, emissivity, and energy partitioning in the impact of irrigation on atmospheric heat content. *J. Appl. Meteorol. Climatol.* 55 (8), 1699–1706.
- Qu, Y., et al., 2015. Mapping surface broadband albedo from satellite observations: a review of literatures on algorithms and products. *Remote Sens.-Basel* 7 (1), 990–1020.
- Rawls, W.J., Ahuja, L.R., Brakensiek, D.L., Shirmohammadi, A., 1993. Chapter 5 In: Maidment, D.R. (Ed.), *Infiltration and Soil Water Movement. Handbook of Hydrology*. McGraw-Hill, New York.
- Román, M.O., et al., 2009. The MODIS (Collection V005) BRDF/albedo product: assessment of spatial representativeness over forested landscapes. *Remote Sens. Environ.* 113 (11), 2476–2498.
- Román, M.O., et al., 2011. Variability in surface BRDF at different spatial scales (30 m-500 m) over a mixed agricultural landscape as retrieved from airborne and satellite spectral measurements. *Remote Sens. Environ.* 115 (9), 2184–2203.
- Román, M.O., et al., 2013. Use of in situ and airborne multiangle data to assess MODIS- and Landsat-based estimates of directional reflectance and albedo. *IEEE Trans. Geosci. Remote. Sens.* 51 (3), 1393–1404.
- Ross, J., 1975. Radiative transfer in plant communities. *Vegetat. Atmosph.* 1, 13–55.
- Rowntree, P., 1991. Atmospheric parameterization schemes for evaporation over land: basic concepts and climate modeling aspects. In: Schmugge, T.A., J.-C (Eds.), *Land Surface Evaporation*. Springer, New York, pp. 5–29.
- Schaaf, C.B., et al., 2002. First operational BRDF, albedo nadir reflectance products from MODIS. *Remote Sens. Environ.* 83 (1-2), 135–148.
- Schmugge, T., French, A., Ritchie, J.C., Rango, A., Pelgrum, H., 2002. Temperature and emissivity separation from multispectral thermal infrared observations. *Remote Sens. Environ.* 79 (2-3), 189–198.
- Sellers, P.J., et al., 1996. The ISLSCP initiative I global datasets: surface boundary conditions and atmospheric forcings for land-atmosphere studies. *Bull. Am. Meteorol. Soc.* 77 (9), 1987–2006.
- Snyder, W.C., Wan, Z., Zhang, Y., Feng, Y.Z., 1998. Classification-based emissivity for land surface temperature measurement from space. *Int. J. Remote Sens.* 19 (14), 2753–2774.
- Song, J., 1998. Diurnal asymmetry in surface albedo. *Agric. For. Meteorol.* 92 (3), 181–189.
- Steven, M.D., Biscoe, P.V., Jaggard, K.W., Paruntu, J., 1986. Foliage cover and radiation interception. *Field Crop Res* 13 (2), 75–87.
- Strugnell, N.C., Lucht, W., Schaaf, C., 2001. A global albedo data set derived from AVHRR data for use in climate simulations. *Geophys. Res. Lett.* 28 (1), 191–194.
- Sun, X., Barros, A.P., 2014. High resolution simulation of tropical storm Ivan (2004) in the Southern Appalachians: role of planetary boundary-layer schemes and cumulus parametrization. *Q. J. R. Meteorol. Soc.* 140 (683), 1847–1865.
- Tao, J., 2015. Understanding the Coupled Surface-groundwater System From Event to Decadal Scale Using an Un-calibrated Hydrologic Model and Data Assimilation (Doctoral Dissertation). Duke University, Durham, North Carolina, USA.
- Tao, J., Barros, A.P., 2013. Prospects for flash flood forecasting in mountainous regions - an investigation of Tropical Storm Fay in the Southern Appalachians. *J. Hydrol. (Amst)* 506, 69–89.
- Tao, J., Barros, A., 2014a. Coupled prediction of flood response and debris flow initiation during warm-and cold-season events in the Southern Appalachians, USA. *Hydroclim. Earth Syst. Sci.* 18 (1), 367–388.
- Tao, J., Barros, A., 2014b. The Integrated Precipitation and Hydrology Experiment. Part I: Quality High-Resolution Landscape Attributes Datasets. Report EPL-2013-IPHEX-H4SE-1, EPL/Duke University (Pub.) 60.
- Tao, J., Barros, A.P., 2018. Multi-year atmospheric forcing datasets for hydrologic modeling in regions of complex terrain—methodology and evaluation over the Integrated Precipitation and Hydrology Experiment 2014 domain. *J. Hydrol. (Amst)* 567, 824–842.
- Tao, J., et al., 2016. Operational hydrological forecasting during the IPHEX-IOP campaign-meet the challenge. *J. Hydrol. (Amst)* 541, 434–456.
- Tesema, Z., Wei, Y., Peel, M., Western, A., 2015. The effect of year-to-year variability of leaf area index on variable infiltration capacity model performance and simulation of runoff. *Adv. Water Resour.* 83, 310–322.
- Trigo, I.F., Peres, L.F., DaCarnara, C.C., Freitas, S.C., 2008. Thermal land surface emissivity retrieved from SEVIRI/meteosat. *IEEE Trans. Geosci. Remote. Sens.* 46 (2), 307–315.
- Wan, Z.M., Li, Z.L., 1997. A physics-based algorithm for retrieving land-surface emissivity and temperature from EOS/MODIS data. *IEEE Trans. Geosci. Remote. Sens.* 35 (4), 980–996.
- Wang, Z., et al., 2004. Using MODIS BRDF and albedo data to evaluate global model land surface albedo. *J. Hydrometeorol.* 5 (1), 3–14.
- Wang, K.C., et al., 2005. Estimation of surface long wave radiation and broadband emissivity using Moderate Resolution Imaging Spectroradiometer (MODIS) land surface temperature/emissivity products. *J. Geophys. Res. Atmos.* (D11), 110.
- Wei, X., et al., 2001. Comparison of albedos computed by land surface models and evaluation against remotely sensed data. *J. Geophys. Res. Atmos.* 106 (D18), 20687–20702.
- Williamson, S.N., Hik, D.S., Gamon, J.A., Kavanaugh, J.L., Koh, S., 2013. Evaluating cloud contamination in clear-sky MODIS terra daytime land surface temperatures using ground-based meteorology station observations. *J. Clim.* 26 (5), 1551–1560.
- Wilson, A.M., Barros, A.P., 2014. An investigation of warm rainfall microphysics in the southern appalachians: orographic enhancement via low-level seeder-feeder interactions. *J. Atmos. Sci.* 71 (5), 1783–1805.
- Wilson, A.M., Barros, A.P., 2017. Orographic land-atmosphere interactions and the diurnal cycle of low-level clouds and fog. *J. Hydrometeorol.* 18 (5), 1513–1533.
- Xiao, Z.Q., et al., 2014. Use of general regression neural networks for generating the GLASS leaf area index product from time-series MODIS surface reflectance. *IEEE Trans. Geosci. Remote. Sens.* 52 (1), 209–223.
- Yang, P., et al., 2007. Evaluation of MODIS land cover and LAI products in cropland of North China plain using in situ measurements and landsat TM images. *IEEE Trans. Geosci. Remote. Sens.* 45 (10), 3087–3097.
- Yeh, G., Cheng, J., 1994. 3DFEMWATER User Manual: a Three-dimensional Finite-element Model of Water Flow Through Saturated-unsaturated Media: Version 2.0. The Pennsylvania State University, University Park, PA.
- Yildiz, O., 2001. Assessment and Simulation of Hydrologic Extremes by a Physically Based Spatially Distributed Hydrologic Model. Ph.D. Thesis. The Pennsylvania State University, University Park, PA, USA.

- Yildiz, O., Barros, A.P., 2005. Climate Variability and Hydrologic Extremes—Modeling the Water and Energy Budgets in the Monongahela River Basin. *Climate and Hydrology in Mountain Areas*. Wiley.
- Yildiz, O., Barros, A.P., 2007. Elucidating vegetation controls on the hydroclimatology of a mid-latitude basin. *J. Hydrol. (Amst)* 333 (2-4), 431–448.
- Yildiz, O., Barros, A.P., 2009. Evaluating spatial variability and scale effects on hydrologic processes in a midsize river basin. *Sci. Res. Essays* 4 (4), 217–225.
- Yuan, H., Dai, Y.J., Xiao, Z.Q., Ji, D.Y., Wei, S.G., 2011. Reprocessing the MODIS Leaf Area Index products for land surface and climate modelling. *Remote Sens. Environ.* 115 (5), 1171–1187.
- Zeng, X.B., 2001. Global vegetation root distribution for land modeling. *J. Hydrometeorol.* 2 (5), 525–530.
- Zeng, X., Shaikh, M., Dai, Y., Dickinson, R.E., Myneni, R., 2002. Coupling of the common land model to the NCAR community climate model. *J. Clim.* 15 (14), 1832–1854.